Large-scale Statistically Meaningful Patterns (LSMPs) associated with precipitation extremes over Northern California

Abhishekh Kumar Srivastava[1*], Richard Grotjahn[1], Alan M. Rhoades[2], Paul Aaron Ullrich[1,3]

[1]University of California, Davis, CA, USA
[2]Lawrence Berkeley National Laboratory, Berkeley, CA, USA
[3]Lawrence Livermore National Laboratory, Livermore, CA, USA

Key Points:

- A significance test finds the minimum number of robust weather pattern clusters for extreme precipitation over Northern California is four.
- How significant and consistent parts of the weather patterns (essential parts of LSMPs) evolve are shown for multiple atmospheric variables.
- Binary forecast skill tests of LSMPs identify variables to use in a new copula-based framework for probabilistic prediction of PEx events.

[*]Department of Land, Air and Water Resources, University of California, Davis, CA, USA

Corresponding author: Abhishekh Kumar Srivastava, asrivas@ucdavis.edu

Abstract

We analyze the large-scale statistically meaningful patterns (LSMPs), also called large-scale meteorological patterns, that precede extreme precipitation (PEx) events over Northern California (NorCal). We find LSMPs by applying k-means clustering to the two leading principal components of daily 500hPa geopotential height anomalies persisting two days before the onset. A statistical significance test based on the Monte Carlo simulations suggests the existence of a minimum of four statistically distinguished LSMP clusters. The four LSMP clusters are characterized as the NW continental negative height anomaly, the Eastward positive "PNA", the Westward negative "PNA", and the Prominent Alaskan ridge. These four clusters, shown in multiple atmospheric and oceanic variables, evolve very differently and have distant links to the Arctic and tropical Pacific regions. Using binary forecast skill measures and a new copula-based framework for predicting PEx events, we show that the LSMP indices are useful predictors of NorCal PEx events, with the moisture-based variables being the best predictors of PEx events at least six days before the onset, and the lower atmospheric variables being better than their upper atmospheric counterparts any day in advance.

Plain Language Summary

Like many other weather extremes, extreme precipitation events can be organized and triggered by large-scale circulation patterns (horizontal span > 1000 km). Often, these circulation patterns evolve in more than one way. In this work, we determine that there are a minimum of four distinct clusters of large-scale circulation patterns that evolve to cause extreme precipitation over Northern California. Although the four clusters have a common low-pressure system persisting near Northern California, they are distinguished from each other in the orientation and spatial extent of low and high-pressure systems over a much larger region. Clusters have different links to properties in distant regions such as: the tropical Pacific Ocean and Alaska as well as regions in between. We constructed indices from statistically significant and commonly-occurring parts of these clusters. Such indices are useful predictors of extreme precipitation events, atmospheric moisture-based variables being the best predictors.

1 Introduction

Extreme precipitation (PEx) over California is marked by a large interannual variability (Dettinger et al., 2011). For example, record rainfall during the winter of 2016-17 was followed by record dry conditions in the fall and winter of 2017-18 (Gershunov et al., 2017). Such a large variability in rainfall is a concern from both drought (Swain et al., 2014; Shukla et al., 2015) and flood perspectives (e.g., Feb 2017 Oroville Dam disaster; White et al., 2019). Projections of future precipitation suggest an increase in high-intensity precipitation extremes and a further enhancement in interannual variability (Swain et al., 2018; Polade et al., 2017; Rhoades et al., 2020). Since changes in PEx over California have severe impacts on activities such as water management, dam protection, agriculture, it is important to understand both the large and small-scale patterns associated with PEx over California. While small-scale local features (e.g., local orography, moisture ascent) pose problems for climate models due to limitations such as inadequate horizontal and vertical resolutions, imperfect parameterizations, cloud microphysics, large-scale circulation mechanisms are largely reproduced in climate model simulations (e.g., Boroneant et al., 2006; Gutowski et al., 2003; DeAngelis et al., 2013; Agel & Barlow, 2020). This study explores the large-scale circulation patterns associated with PEx events over Northern California (NorCal).

Large-scale meteorological patterns, also called Large-scale Statistically Meaningful Patterns (LSMPs), associated with extreme events are the synoptic-to-large-scale atmospheric and surface conditions that precede the events (e.g., PEx or temperature events,

or cold-air outbreaks). LSMPs are different from teleconnections (e.g., the El Niño Southern Oscillation) in several ways. First, LSMPs can be high-frequency patterns based on instantaneous data (as in this report). Second, LSMPs are the specific meteorological patterns that occur in connection with an extreme event type, whereas teleconnections are recurring, slowly-evolving, persistent, large-scale patterns (also known as low-frequency modes of variability) that can be defined without any reference to extremes (Barlow et al., 2019). While local factors such as lifting, static stability, and moisture availability control the intensity and duration of PEx (e.g., Neiman et al., 2002; Moore et al., 2020), LSMPs that determine or control these factors vary with season, region, and definition of an extreme event.

As outlined in Grotjahn et al. (2016), multiple methods can identify large-scale circulation features associated with an extreme event. A common method is the construction of composited maps of meteorological variables conditioned on the occurrence of an extreme event type (Grotjahn & Faure, 2008; DeAngelis et al., 2013; Gao et al., 2014; Collow et al., 2016, 2020). Compositing-based studies show that the precipitation days over NorCal are locally associated with a low-pressure system and associated extratropical cyclones in the Northern Pacific off the west coast of the United States (e.g., Grotjahn & Faure, 2008; Neiman et al., 2008; Gao et al., 2014). These weather systems act to channel winds and moisture into narrow structures called atmospheric rivers (Ralph et al., 2006) that are directed towards the coast to produce precipitation over land (Smith et al., 2010). Another strong feature of these large-scale patterns is the zonally elongated jet over the North Pacific further extended towards the west coast of the United States (Payne & Magnusdottir, 2014).

However, when looking at large scales, locally persistent low-pressure systems are found to be embedded in different circulation patterns, suggesting that there could be more than one large-scale pattern that can be associated with PEx events over NorCal. Popular methods that can identify these different circulation features are: empirical orthogonal function (EOF) analysis (Guirguis et al., 2018, 2020), self-organizing maps (SOMs; Loikith et al., 2017; Guirguis et al., 2019), and clustering analysis (Agel et al., 2018; Zhao et al., 2019; Moore et al., 2021). Loikith et al. (2017) demonstrated that the majority of the PEx days over the western United States occur with their SOM node 1, identified by a surface low pressure centered to the northwest of the northwestern continental United States, a 500mb geopotential height (Z500) trough axis offshore, and the main axis of the 250mb jet zonally oriented over central California. Guirguis et al. (2020), using SOM analysis, demonstrated that wet and dry conditions over California result from interactions between four North Pacific circulation regimes (their NP4 regimes) on daily timescales. D. Chen et al. (2021) found that the third principal component of the Z500 field has a strong positive correlation with the Z500 anomalies existing off the northwestern United States coast during PEx events that occur in California. Guirguis et al. (2019) applied SOMs to Z500 anomalies to find nine nodes associated with peak atmospheric river (AR) days at 40°N impacting NorCal. They showed that these nodes occur during different phases of large-scale teleconnection patterns such as El Niño-Southern oscillation (ENSO), Pacific decadal oscillation (PDO), and Pacific North American (PNA) pattern. Moore et al. (2021) found four categories of large-scale atmospheric patterns for long-duration (> 7 days) heavy precipitation events over the West Coast of the United States. Out of these four categories, two are identified by a strong zonal jet stream over the eastern North Pacific, and the two other patterns are identified by atmospheric blocking over the central North Pacific and the Bering Sea–Alaska region, respectively.

These studies provide useful information about how PEx forms over NorCal. Nonetheless, there are five aspects of research methodology to consider. First, there is a misconception about what constitutes an LSMP. As elaborated in Grotjahn (2011), an LSMP of a *relevant* variable, often meteorological (e.g., 500 mb geopotential height anomaly field) is more than some aggregate field; it also must indicate what is important in the

field. Therefore, *an LSMP includes two additional integral features: significance and consistency.* The significance establishes if an anomalous pattern (e.g., sea surface temperature anomaly) statistically differs from what occurs by chance. Consistency, as the name suggests, refers to how often an anomaly of the same sign occurs at a grid point or location. Previous studies showing aggregate patterns often overlook the consistency assessment. We argue that significance and consistency are integral parts of an LSMP for two reasons: a) high significance does not guarantee high consistency (e.g. Grotjahn and Faure (2008) and b) any future changes in either significance or consistency may suggest dynamical changes impacting the occurrences of extremes. Second, a majority of previous studies have considered a small spatial domain around NorCal. However, as the name suggests, LSMPs are large-scale patterns (and may show far teleconnections, too) that may not be fully captured by such small domains. Third, what is the minimum number of LSMP clusters necessary to best describe northern California's PEx events? This question has direct relevance for climate model evaluation, as any model expected to reasonably simulate PEx should be able to reproduce the spatial pattern and frequency of each observed clustered pattern. Fourth, most studies use concurrent meteorological conditions (same day) for identifying and clustering large-scale patterns associated with PEx events (e.g., Barlow et al., 2019). Analogous to NorCal heat waves, which have a similar pattern at their onset that is arrived upon from two different synoptic evolutions (Lee & Grotjahn, 2016), NorCal PEx events might also be arrived at by more than one synoptic evolution. Indeed, Figure 6 in (Grotjahn & Faure, 2008) implies more than one pattern as individual events have a highly significant Alaskan ridge while other events have a deep trough over Alaska. From causal and predictability perspectives, the relevant LSMPs should be identified from the meteorological conditions persisting before the event. Fifth, although a limited number of studies have shown the predictability of PEx events using LSMPs as predictors (e.g., Gao & Mathur, 2021), a comprehensive approach for probabilistic predictions of precipitation using LSMPs as predictors is missing.

In this work, we examine the LSMPs associated with PEx over NorCal to address the limitations mentioned above. A PEx event is defined here as the 24-hour precipitation total of more than the 95^{th} percentile of the daily precipitation averaged over a region of NorCal. We also present a copula-based framework for making probabilistic predictions of precipitation. Broadly, our main objectives are:

1. identify clusters of LSMPs that persist before the onset of the PEx over NorCal;
2. statistically estimate the minimum number of distinguishable LSMP clusters leading to PEx events over NorCal;
3. examine the evolution of a comprehensive list of meteorological LSMPs leading to the PEx event onset;
4. use a copula-based framework to make a probabilistic prediction of PEx events over NorCal using LSMP indices as predictors.

The LSMP clusters are identified by applying the k-means clustering algorithm to the two leading principal components of the 500hPa daily geopotential height anomalies (Z500) two days before the onset (lag 2). Along with the Z500, we show the evolution of LSMPs associated with the other related quantities such as 850hPa and 200hPa velocity fields, streamfunctions at 200 and 850mb, surface temperature, integrated vapor transport (IVT), and surface pressure.

This paper strongly complements the paper by Moore et al. (2021), which focused on synoptic dynamics during 7-day-long PEx events impacting NorCal. Here, we focus on predictability, remote connections, and the creation of 1-day or longer PEx events impacting the same region. While they include all events, we include only the largest precipitation day in a multi precipitation day event and exclude "mixed" events which cannot be clearly assigned to a single cluster. We do this to have more distinct clusters and are enabled to do so because we have larger sample sizes. Our patterns are sharper be-

cause we are combining "instantaneous" fields, not time averaging, during which multiple weather systems move across the domain. We also employ a rigorous test to see the minimum number of clusters needed for them to be significantly different. We search for LSMPs over a larger region and, in so doing, find distant connections not found within their original focus region. While they present the significant parts of patterns, we apply a true LSMP analysis and also measure consistency since it is critical for assessing predictability. Following this introduction, the data and methods are discussed in section 2, results in section 3, and an overall summary is in section 4.

2 Data and Method

In this study, we use daily $0.25° \times 0.25°$ precipitation data over 1948-2015 from the National Oceanic and Atmospheric Administration Climate Prediction Center (CPC) Unified CONUS dataset (CPC; Xie et al., 2007; M. Chen et al., 2008) to identify PEx events over the NorCal region. The gridded CPC data are constructed from the quality-controlled station data using the optimal interpolation (OI) algorithm, which exhibits relatively small degradation in performance statistics over regions covered by fewer gauges. To identify extreme precipitation events, we first calculate the 24-hour spatially averaged precipitation $\bar{P}$ by taking the mean of 24-hour non-zero precipitation values (i.e., $P > 0$ mm/day) at each grid point across the NorCal region defined as 124.5°W to 119.25°W and 38.69°N to 43.17°N. A PEx event is identified if a 24-hour $\bar{P}$ magnitude exceeds the 95^{th} percentile of $\bar{P}$ values over 1948-2015. This criterion identifies a total of 489 daily precipitation events. However, some of these events are on consecutive days. Since such events on consecutive days are not exclusively independent, we pick the largest precipitation day in a 3-day period. This procedure reduces the total number of exclusive events to 311.

For the LSMP analysis, we use the NOAA–CIRES–DOE Twentieth Century Reanalysis version 3 (20CRv3; Slivinski et al., 2019). The 20CRv3 uses an Earth system model to assimilate surface pressure observations with prescribed lower boundary conditions from observed sea surface temperature and sea-ice concentrations and bounded by prescribed radiative forcing to generate a four-dimensional global reanalysis product. Compared to its predecessor, 20CRv2c, the 20CRv3 uses upgraded assimilation methods, including an adaptive inflation algorithm, a higher resolution forecast model and a larger set of pressure observations. These improvements remove spin-up effects in the precipitation fields, reduce sea-level pressure bias, and improve the representation of storm intensity in the reanalysis product (Slivinski et al., 2019).

In this study, we analyze the following variables from 20CRv3: surface pressure (P_s), surface temperature (T_s), integrated vapor transport (IVT), horizontal and vertical velocity fields (U, V, ω), atmospheric temperature (T), geopotential height (Z) and streamfunction (ψ) at 200, 500 and 850hPa levels. We compute the daily anomalies of these variables by simultaneously regressing out the annual cycle and linear trend from the daily data over the period 1948-2015. Though not shown here, this approach of removing the annual cycle and trend from the data ensures that no residual trend or annual cycle remains present in the final anomaly product.

2.1 Clustering Procedure

For the clustering analysis, we apply a k-means clustering algorithm to the two leading principal components (PCs) of the 500hPa geopotential height anomalies two days before (lag 2) (Za_{l2}^{500}) the event onset. The cluster domain is 180°W to 100°W and 25°N to 75°N. The two leading PCs explain around 54% of the variance. We estimate the significance of clusters using a Monte Carlo procedure following Straus (2018), described as follows. For each chosen number of clusters ($k = 1, 2, 3 \ldots$ etc.), we compute the variance ratio ($R = \Delta/S$) for the first two PCs of Za_{l2}^{500}, where, Δ is the spread among the

cluster centroids (also called between-sum-of-squares) and S is the spread within clusters (also called total-within-sum-of-squares). In cluster analysis, we seek to minimize the spread within clusters, S. A maximum of the variance ratio R corresponds to a minimum of S. We repeat the above-mentioned procedure 100 times with synthetic datasets. The synthetic datasets are generated from the multivariate Gaussian distribution computed using the same mean and covariance as in the data (here, the two leading PCs). For each iteration, we compute $R_{sample} = \Delta/S$. Finally, the 99^{th} percentile of the 100 R_{sample} values, (R_{sig}) is computed. If $R > R_{sig}$ for a particular k, the clusters are declared significant and different from those occurring by chance. This procedure is repeated for $k = 1 : 7$. A similar procedure is also applied in Amini and Straus (2019). This process leads us to identify 4 significant clusters of Za_{l2}^{500}. For simplicity, we call the clusters LZ_{l2} to indicate that the clusters are formed from Za^{500} fields at lag 2. For each cluster, the cluster centroid $(\overline{LZ}_{l2}^{c})$ is computed by taking the mean of all cluster members $1 \dots n_c$:

$$\overline{LZ}_{l2}^{c} = \frac{\sum_{n=1}^{n_c} Za_{l2,n}^{500}}{n_c}, \tag{1}$$

where, $\sum$ denotes summation over all cluster members, $n = 1 \dots n_c$, in a cluster c.

2.2 Construction of LSMP indices

We construct a daily LSMP index (LSMPi) for each meteorological variable mainly to make probabilistic predictions of precipitation. First, we choose a spatial domain that captures the highly significant and consistent regions for the LSMPs. A large domain was used to ensure that we capture the full spatiotemporal extent of the LSMPs. For the LSMPi, unimportant regions are excluded and the domain is smaller: 180° to 100°W and 25°N to 75°N. Then we divide the years under consideration into training (NDJFM of 1948-1982) and verification years (NDJFM of 1982-2015). Corresponding to the training and verification periods, we divide all meteorological fields (Y) into training (Y^T) and verification (Y^V) sets. Then, we construct "training" LSMPs for a variable Y^T, $\overline{LY}_{l*}^{c,T}$ for each cluster c as in Eqn. 1, where $*$ denotes lags 0-6. The LSMPi for a meteorological variable (Y^T) in the training period T is constructed by projecting $\overline{LY}_{l*}^{c,T}$ onto the corresponding daily (Y^T) timeseries,

$$LSMPi_{Y}^{c,T} = \frac{(W\overline{LY}_{l*}^{c,T})(WY^T)}{[W\overline{LY}_{l*}^{c,T}]^2}, \tag{2}$$

where W is the weight assigned to each grid point based on both the normalized sign count and areal weighting accounting for the convergence of meridians: $LSMPi_{Y}^{c,T}$ is the daily product having dimensions of $lon \times lat$ for each cluster. The final daily LSMPi $(LSMPi_{Y}^{T})$ is chosen by taking the maximum of the 4 $LSMPi_{Y}^{c,T}$.

Similarly, the LSMPi for a meteorological variable (Y^V) in the verification period V is constructed by projecting $\overline{LY}_{l*}^{c,T}$ onto the corresponding daily Y^V time series,

$$LSMPi_{Y}^{c,V} = \frac{(W\overline{LY}_{l*}^{c,T})(WY^V)}{[W\overline{LY}_{l*}^{c,T}]^2}, \tag{3}$$

The final daily LSMPi $(LSMPi_{Y}^{V})$ is constructed by taking the maximum of the four $LSMPi_{Y}^{c,V}$. We use the same training LSMP $\overline{LY}_{l*}^{c,T}$ to compute LSMPi for training and verification datasets. The daily LSMPi measures how similar a given day is to a specific cluster mean LSMP.

2.3 Probabilistic prediction of precipitation events using LSMP indices

We now show that the daily LSMPi of meteorological variables are skillful predictors of PEx events. The LSMPi for each variable is constructed as described in section 2.2. To find useful predictors, we use quantile regression to predict the 95^{th} percentile of $\overline{P}$ using LSMPi as predictors. The fitness of each LSMPi predictor is estimated using a model selection criterion called the Akaike information criterion (AIC; Akaike, 1974). We also use a combination of two or more predictor variables to estimate if it produces a lower AIC than the individual AIC values. A suite of measures for assessing the prediction skill of LSMPi is used and associated with different meteorological variables. These measures of prediction skill are described in Table 1.

Table 1: Contingency table and measures of prediction skills. The observed and forecasted events are PEx $> 95^{th}$ percentile.

(a) Contingency Table

Forecast	Observed		Marginal Total
	Yes	No	
Yes	(a) Hit	(b) False Alarm	a+b
No	(c) Miss	(d) Correct Negative	c+d
Marginal Total	a+c	b+d	a+b+c+d

(b) Prediction Measures
$a^* = \frac{(a+b)(a+c)}{(a+b+c+d)}$

Measures	Formula	Range [poor – good]
Probability of Detection (POD)	$\frac{a}{(a+c)}$	[0,1]
False Alarm Ratio (FAR)	$\frac{b}{(a+b)}$	[1,0]
Threat Score (TS)	$\frac{a}{(a+b+c)}$	[0,1]
Gilbert Skill Score (GSS)	$\frac{(a-a^*)}{(a-a^*+b+c)}$	$[-\frac{1}{3},1]$; no skill = 0
Pierce Skill Score (PSS)	$\frac{(ad-bc)}{(a+c)(b+d)}$	[-1,1]; no skill = 0

Of the atmospheric variables tested, we find that IVT at lag 2 is the best predictor of a PEx event, and adding any other variable to IVT does not significantly reduce the AIC. Therefore, we use LSMPi for IVT from the training and verification sets to make probabilistic predictions of precipitation. We use a copula framework to make a probabilistic prediction of PEx events. Copulas are mathematical functions that define the joint distributions of two or more random variables independent of their marginal distributions (AghaKouchak et al., 2010; Hao & AghaKouchak, 2013; Shojaeezadeh et al., 2018). We use a copula to define the conditional probability density of precipitation using the marginal distributions of an LSMPi and the joint distribution of the LSMPi and daily precipitation, as summarized below:

If $F(p) = y$ and $F(l) = x$ are marginal conditional distribution functions (CDFs) of daily precipitation (P) and an LSMPi (l), then there exists a copula function (C) that defines their joint CDF,

$$F(p, l) = C(F(p), F(l)) = C(y, x). \tag{4}$$

The copula probability density function c(*) can be defined as:

$$c(y,x) = \frac{\partial^2 C(y,x)}{\partial y \partial x}. \tag{5}$$

From (4) and (5), the conditional probability of precipitation (P) conditioned on the LSMPi (l) is defined as

$$f(p|l) = c(y,x) f(l), \tag{6}$$

where $f(l)$ is the PDF of the LSMPi(l).

3 Results

3.1 Indentifying minimum number of clusters using k-means clustering

As mentioned in the methods section, we apply a k-means clustering (kmc) algorithm to the 2 leading PCs of Za_{l2}^{500} and compute the variance ratio as described in the methods section. The resulting variance ratio R for 1 to 7 clusters is shown as a black curve in Fig. 1(a). We also compute the variance ratio for the synthetic data as described in the methods section; the 99^{th} percentile of which (R_{sig}) is shown as the red dashed curve. A cluster number is considered significant at the 99% level if $R > R_{sig}$ (i.e., where a black circle is above the red line in Fig. 1a). The figure suggests that a set of 3 clusters or more is statistically significant at the 99% significance level. To find the minimum number of robust clusters, we also perform a series of sensitivity tests to varying event detection criteria (e.g., varying precipitation threshold) and multiple spatial domain sizes. We find that a minimum of 4 clusters is statistically significant and robust. In addition to the significance and sensitivity tests, we also visually examined the cluster mean Za^{500} patterns for k=3, 4, and 5 as depicted using map plots in Fig. 1(b). In the figure, the patterns for k=3 are as follows. The first pattern is identified by a northwest-to-southeast oriented wavetrain with a large positive height anomaly centered over the Aleutian Islands and adjacent ocean. The second cluster is identified by a large negative anomaly centered over Alaska and along the west coast of North America, plus positive anomalies to the southwest and east. The third cluster has a roughly North-South-oriented pattern of positive anomaly over Alaska, negative over the eastern North Pacific, and a weak positive extending from the subtropical eastern Pacific to Baja California. To identify each pattern for different k clusters, we label each with a colored oval: solid yellow, long-dashed blue, small dashed orange clusters, respectively. As we go down a row to larger k, we must add a new cluster, and that new cluster is often a subset of a cluster identified from the row above. When going from k=3 to 4, we can find the solid yellow, long-dashed blue, small-dashed orange clusters again. However, the second cluster seems to be different, so we give it a new color, dot-dashed pink. As we go to 4 clusters from 3, we can see that several clusters, such as the small-dashed orange one, have a more sharply defined pattern than their counterparts when k=3, including larger sign counts. Therefore, we posit that k=4 is an improvement over what we have for k=3. When we go from k=4 to 5, we observe some similar patterns again, with a combination of long-dashed blue, dot-dashed pink, solid yellow and small-dashed orange k-clusters. However, we have a new pattern (i.e., the second cluster). A close visual inspection reveals that the new cluster is very similar in characteristics (i.e., Za500 magnitude, sign, and gradients) to the dot-dashed pink and long-dashed blue clusters. Thus, we assume that going from cluster numbers 3 to 4, we gained value since we identified stronger cluster members. But, in going from k=4 to 5, the "new member" does not provide a distinctly different meteorological pattern and thus does not add significant value to our understanding. Therefore, we make a subjective, but justified decision to stop at 4 clusters. From this analysis, we conclude that a minimum of 4 cluster patterns can contain compactly all the possible meteorological patterns associated with the NorCal precipitation extremes. Any additional cluster (say, k=5) produces a pattern that is not sufficiently different from previous clusters and is less informative than for k=4.

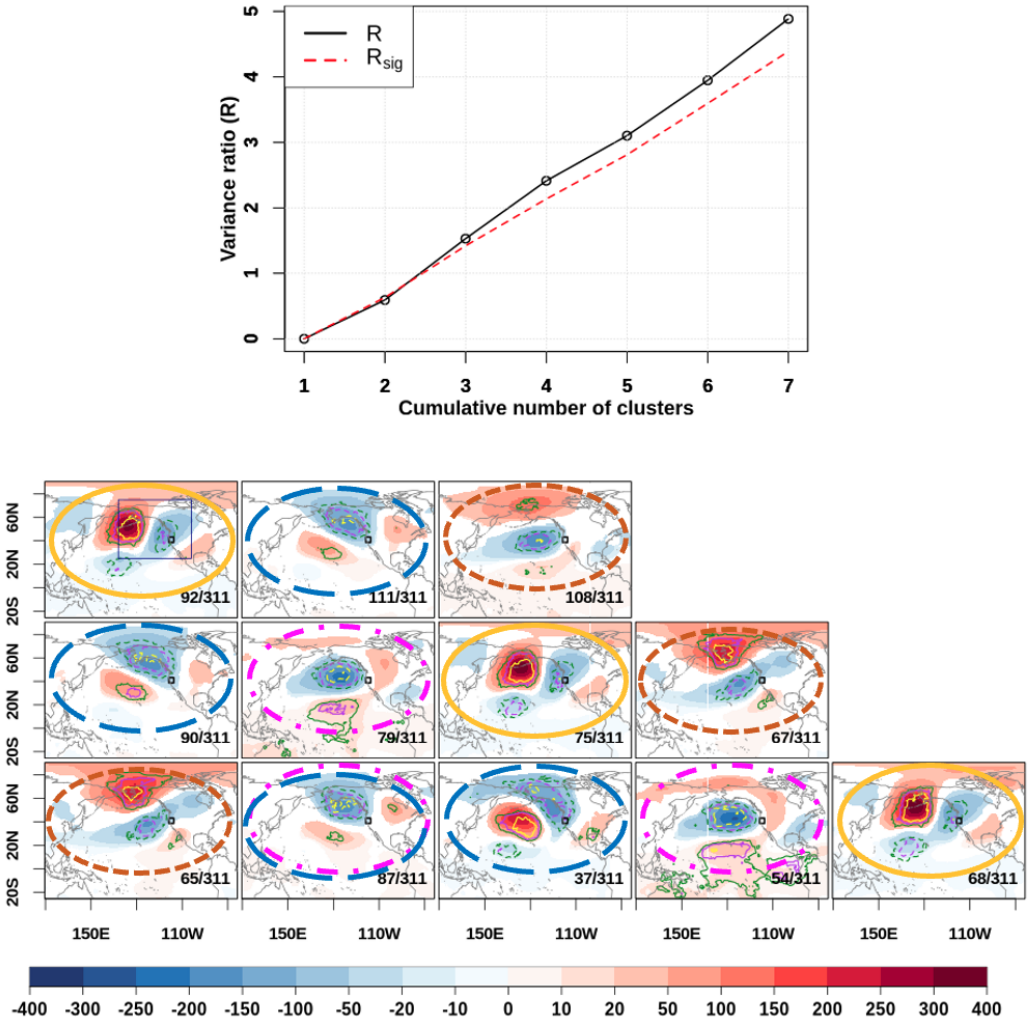

Figure 1: (a): Significance of Za_{l2}^{500} clusters for cluster numbers 1 to 7. The X-axis shows the number of clusters for which the variance ratio (R) on the Y-axis is computed. The black curve shows variance ratio R computed from Za_{l2}^{500}. The red curve shows the 99^{th} percentile (R_{sig}) of the variance ratio computed from synthetic data generated using the Monte Carlo procedure. A cluster number is considered significant if $R > R_{sig}$. (b): Clustering of 500hPa geopotential height anomalies, Za_{l2}^{500} at lag 2. Top row: k=3, Middle row: k=4, Bottom row: k=5. Shaded contours are plotted where significant at the 95% level. The small square over Northern California on each panel is the NorCal region where the PEx occurs two days later. The ratio in the lower right corner of each panel shows the number of events in that cluster divided by the total number of events. Line contours show consistency via sign counts, where green equals 0.6 (meaning 80% of the ensemble members have the same sign at that point). Purple is 0.75 (87.5%) and yellow is 0.9 (95%). The colored ovals indicate the most similar pattern across different rows. However, three of the panels on the bottom row seem subjectively to mix two patterns on the middle row. In the top-left panel, the navy-colored rectangle shows the domain used for the clustering analysis.

The k-means clustering was applied to 311 events and the result is in Fig. 1(b). The k-means clustering is a hard clustering method, in that each member is entirely assigned to a cluster. However, events may resemble more than one cluster. In such cases, the membership of that event is not unequivocally defined. In an iterative procedure, we identified those mixed cases and removed them from the final clustering. This procedure further reduces the events from 311 to 243. The final cluster mean patterns in Za^{500} using 243 events are shown in Fig. 2. The k-means clustering divides the 243 precipitation events into 4 clusters of roughly equal sizes. Clusters 1-4 have 71, 70, 61, and 41 members, respectively. Moore et al. (2021) applied fuzzy clustering to identify clusters of meteorological variables associated with Northern California PEx events. Fuzzy clustering assigns probability values to each member of the cluster. This allows any individual member to belong to more than one cluster. Our procedure ensures that only those members that have similar probabilities of being in more than one cluster are removed from the final set of clusters.

The LSMP patterns shown here are similar to patterns shown in Moore et al. (2021). Using two EOFs of Za_{l2}^{500}, they find four patterns, as well. However, their patterns are derived from time averages of the first five days of long-duration PEx events. Here, we show patterns two days *prior* to PEx event onset and include many more shorter-duration events. Noting these differences, our four clusters have analogs with their four clusters. Specifically, our clusters 1-4 are most similar to their clusters C2, C1, C3, and C4, respectively. Our names for the patterns differ from those used by Moore et al. (2021) because: a) we examine the patterns over a larger domain and b) we emphasize the properties of the field used to define the clusters.

Our four identified clusters are as follows. (For comparison, Moore et al. (2021) names are in parentheses.)

1. *Northwest continental negative height anomaly* (Poleward-shifted zonal jet) Cluster 1 has a large negative Za^{500} that extends over Alaska and the west coast of North America. Southwest of it, a positive anomaly occupies the midlatitude Pacific. Also present is a faint but significant positive anomaly over northeast North America. However, the latter positive anomaly has a low consistency from the sign count.
2. *Eastward positive "PNA"* (Equatorward-shifted zonal jet) Cluster 2 has a large negative geopotential anomaly centered over the northern Pacific co-occurring with a positive Za^{500} to the south over the central tropical Pacific (between 20°N and 20°S). Also present are significant, weak, low sign count positive central Canadian and negative SE USA anomalies. Together the four anomalies look somewhat similar to the Pacific-North American (PNA; Wallace & Gutzler, 1981; Barnston & Livezey, 1987; Leathers et al., 1991) loading pattern, except that it has been phase shifted eastward. "PNA" in the cluster label is purely descriptive of the pattern and not intended to be equal to the actual PNA pattern. The pattern elements are a north-south anomaly pair in the Pacific and a wavetrain extending eastwards then southwards from that negative, strong, NE Pacific negative anomaly.
3. *Westward negative "PNA"* (Midlatitude blocking) Cluster 3 has a Northwest-Southeast wavetrain with a very strong positive anomaly centered over the Aleutian region with a strong negative anomaly near the Canadian west coast. Also co-occurring is a low in the central subtropical Pacific and a weak, low sign count, positive anomaly over southeastern North America. These four anomaly centers have some similarity to the PNA pattern (with a negative sign), though parts of this cluster average are shifted westward relative to the actual PNA loading pattern. Again, "PNA" in the label is purely descriptive. This pattern is very similar to the California cold air outbreak (CAO) pattern (Grotjahn & Zhang, 2017) two days before the CAO, but here shifted $\sim$ 10 degrees west.

4. *Prominent Alaskan ridge* (High-latitude blocking) Cluster 4 has a prominent positive anomaly over Alaska and the adjacent Arctic Ocean. To the south-southeast, lies a negative anomaly and further south-southeast a weak positive anomaly extending across much of the tropical Pacific to subtropical Baja California.

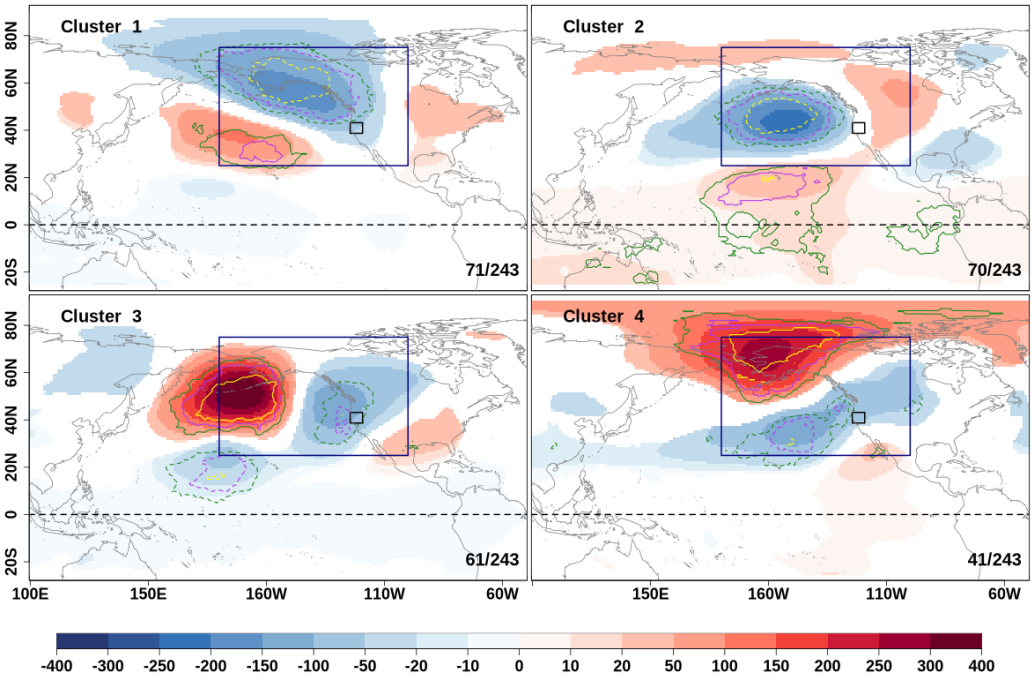

Figure 2: LSMP clusters of Za_{l2}^{500} (unit: m) two days prior to the PEx onset in a format similar to individual panels of Figure 1(b). Events identified as "mixed" have now been removed from the analysis leaving 243 events tracked. The ratio in the lower right corner of each panel shows the number of events in that cluster divided by the total number of events tracked. Line contours show consistency via sign counts, where green means 80% of the ensemble members have the same sign at that point, purple is 87.5%, and yellow is 95%. The navy-colored large rectangle shows the domain used for the clustering analysis. The small black rectangle indicates the NorCal region. A dashed line marks the equator.

Three broad conclusions can be drawn to this point. First, several prior works listed in the introduction looked at a smaller region, and all find a low pressure centered off the California coast. We also find an anomalous low pressure just off the coast in all of our PEx events. But, this low differs greatly in shape between the clusters. Second, this low is part of a much larger-scale pattern that can be grouped into four clusters. The spatial patterns associated with the PEx clusters extend over much of the North American continent and northern Pacific, even across the equatorial Pacific. Significant patterns over the tropical Pacific suggesting a tropical connection to rainfall extremes over Northern California. Third, each cluster mean in Fig. 2 has patterns that are statistically significant (shading) and highly consistent (contours), making the patterns true LSMPs.

3.2 Evolution of Clusters

How do these LSMPs form and evolve? This subsection describes the concurrent evolution of cluster mean meteorological fields during the fortnight before PEx onset.

Notably, some clusters can be traced backward in time much longer than other clusters. The figure descriptions are included to identify important features from which generalizations will be drawn. There are multiple potential uses for these LSMP details, such as: dynamical analysis, model assessment, model projections, and predictability. Probabilistic prediction is explored in section 3.3.

To sample LSMP properties the following figures are discussed. Fig 3 shows 500 hPa streamfunction anomalies (Ψa^{500}); this field captures the patterns of atmospheric highs and lows and consequent flow, but is preferable to geopotential height for depicting flow patterns in the tropical and equatorial regions. The upper-level jet evolution is shown, with a focus on the zonal component at 200 hPa (Ua^{200}, Fig. 4) supplemented by information from the meridional wind anomaly component (Va^{200}) in Fig. S1. We show the evolution of vertically-integrated water vapor transport, IVTa in Fig. 5. Local minima in mean sea level pressure anomaly ($SLPa$, Fig. 6) are used to indicate the position of cyclones (Wernli & Schwierz, 2006), which guide low-level water vapor fluxes towards NorCal. We also show the evolution of lower tropospheric temperature in Fig. 7. This field is often used for statistical downscaling of precipitation and therefore may be a potential predictor of PEx events.

3.2.1 Evolution of 500hPa streamfunction anomalies ($\Psi\mathbf{a}^{500}$)

The evolution of 500hPa streamfunction anomalies (Ψa^{500}) for the four clusters is shown in Fig. 3. Ψa^{200} and Ψa^{850} are similar to that for Ψa^{500}, and hence are not shown.

The cluster 1 pattern starts with a central North Pacific ridge anomaly roughly a half dozen days before the event onset. This ridge anomaly extends throughout the atmospheric column (being visible at 200 and 850 hPa levels). Northeast of it, a trough builds over Alaska and beyond: from NorCal northwestward to the Bering Strait. This low anomaly is very large and mainly over the continent, hence our label of NW continental negative anomaly. That huge trough anomaly is strongest the last two days before onset. At onset, a weak ridge anomaly forms over southwestern North America. This combination of anomalies, trough northwest and ridge southeast of the PEx region, supports a strong onshore flow over the PEx region.

Cluster 2 has a pair of anomalies: a mid-latitude trough centered near 50°N and a subtropical ridge near 20°N that emerge in the North Pacific almost two weeks before PEx onset. Both anomalies grow in size and strength over a fortnight, with the slight eastward movement of the ridge-trough pattern. The orientation and location of the ridge-trough pattern in cluster 2 both differ from cluster 1, such that the trough anomaly in cluster 2 is located further south, over the North Pacific Ocean and partly over southwestern Canada. This trough anomaly is strongest two days before onset. Also, the trough-ridge pattern in cluster 2 is oriented more N-S than in cluster 1.

In cluster 3, a stationary Aleutian ridge anomaly is observed in the 200, 500, and 850 hPa Ψa fields more than a week before onset, steadily strengthening until peak anomaly amplitude two days before onset. Two Ψa^{500} troughs develop, one to the south and the other to the east of the Aleutian ridge anomaly around a week before the onset. A secondary ridge in Ψa^{500} forms over northern Mexico and Southern CONUS a few days before the onset. This secondary anomalous ridge is much stronger and wider than in the two prior clusters. The four strong anomaly centers are superficially similar to the PNA pattern, but the whole pattern is shifted west by >20 degrees of longitude, thus prompting our label of Westward negative "PNA".

For cluster 4, a high anomaly Ψa^{500} starts developing over northern Alaska about 8 days before PEx onset. This ridge prompts our cluster label: Prominent Alaskan ridge. This ridge anomaly expands westward until the onset, but it reaches peak amplitude over northern Alaska two days before onset. A low forms over the central North Pacific a few

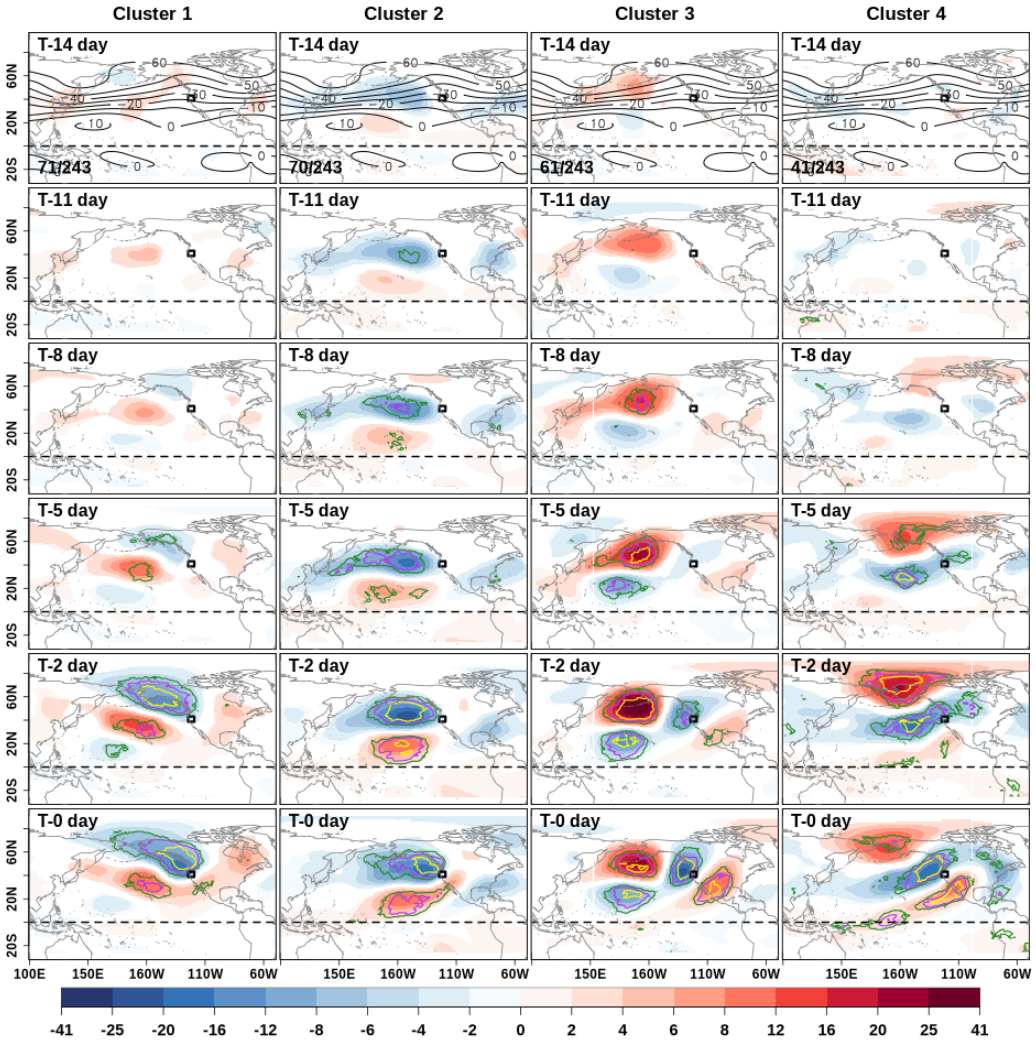

Figure 3: Evolution of 500hPa streamfunction anomalies (unit:$10^6 m^2/s$). Shaded areas show anomalies significant at the 5% level. Contours show the consistency of the anomaly pattern. Green, magenta and yellow contours show that at least 80%, 87.5%, and 95% of the cluster members have the same sign of anomalies, respectively. Solid black contours (contour interval: $10 \times 10^6 m^2/s$) in the top row show the climatological total streamfunction. The ratio in the lower-left corner of each top row panel shows the number of events in that cluster divided by the total number of events. The black rectangle indicates the NorCal region. A dashed line marks the equator.

days later, which expands eastward across the North American west coast, forming a band of low pressure anomaly extending from the tropical Pacific Ocean across to north-central Canada. A secondary ridge anomaly is again centered over northern Mexico 2 days prior to the onset and appears to extend southwestward to Papua New Guinea. Together, the anomalies form a ridge-trough-ridge pattern along the North American west coast.

In all four clusters, the most prominent and distinguishing features of each LSMP reach *peak amplitude, significance, and consistency two days before onset*. Furthermore, the cluster means differ less at onset than two days before; therefore, the best time for defining an LSMPi *that separates the clusters* is two days before onset.

3.2.2 Evolution of Upper-level jet (Ua^{200})

The evolution of 200hPa zonal wind anomaly field (Ua^{200}) is shown in Fig. 4. The meridional component wind anomaly at 200 hPa (Va^{200}) is shown in the supplemental material Fig. S1.

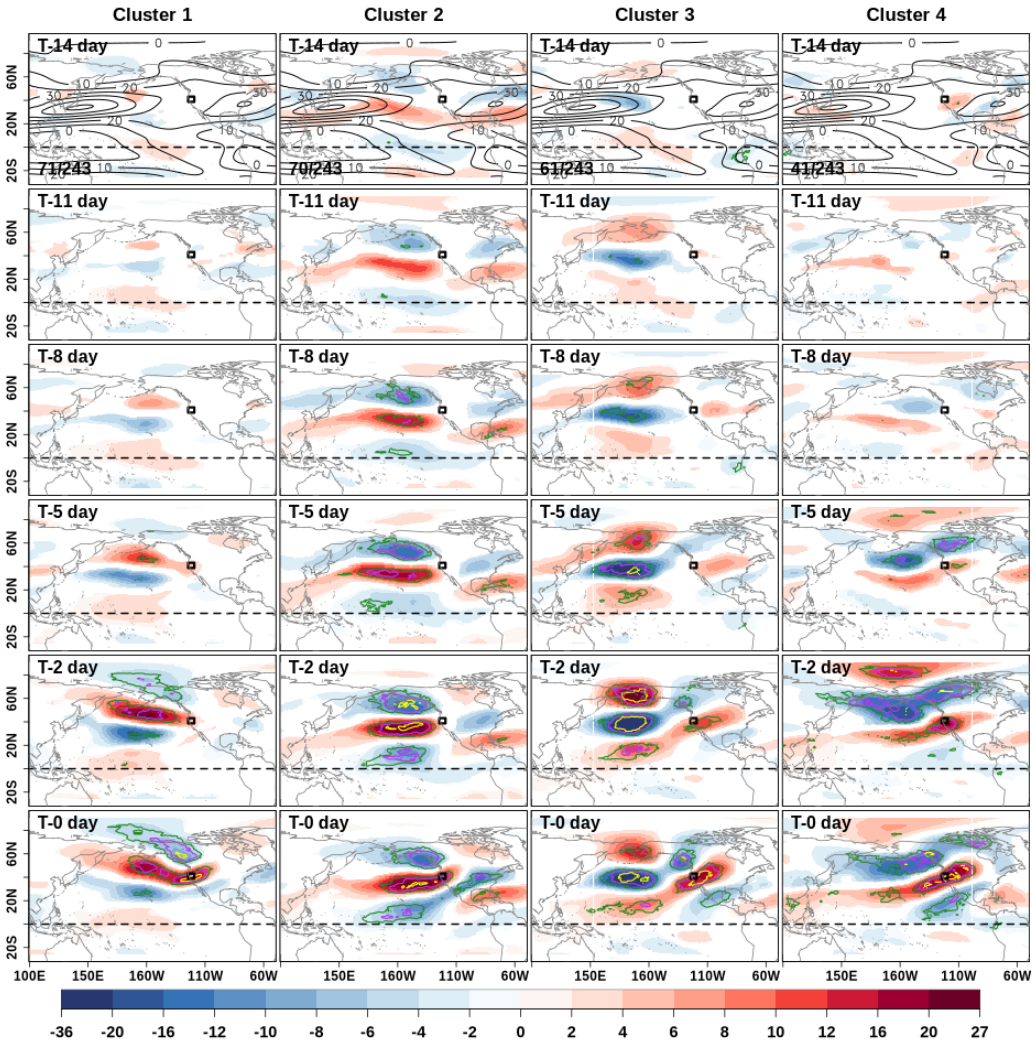

Figure 4: Same as Fig. 3 but for the evolution of 200hPa zonal wind anomalies (unit: m/s). Solid black contours (contour interval: 10 m/s) in the top rows show the climatological total zonal wind.

For cluster 1, beginning about 5-7 days prior to onset, there is a prominent dipole across much of the North Pacific. This dipole is centered mainly on the downstream end of the Asian subtropical jet. The effect of the dipole is to build the north side and reduce the south side of the jet, mid-Pacific. As onset approaches, another negative anomaly (over northwest North America) appears. That negative anomaly along with the increasing amplitude and eastward extension of the positive anomaly results in a narrowing and dramatic strengthening of the jet over our NorCal focus region. Onshore zonal winds exceed 25 m/s at the focus region with an orientation that is from the southwest. The Va^{200} pattern (supplemental material Fig. S1) shows comparable southerlies at and north of the NorCal region, giving the jet a SW-NE orientation there. The LSMPs are approximately equivalent-barotropic. Hence, the anomaly pattern for a wind anomaly component is similar at all levels from 850 through 200hPa.

In cluster 2 the 200hPa streamfunction of Fig. 3, shows the NorCal region is sandwiched between a deep low to the north and a narrow ridge to the south at the onset. Hence, zonally-elongated 200hPa zonal wind anomalies are oriented southwest-northeast up to two days before onset. A tripolar pattern by day 2 is similar to that in cluster 1, except the meridional spread is larger. A result is the positive anomaly of cluster 2 is nearly at the same latitude as a negative anomaly in cluster 1. Also unlike cluster 1, these anomalies are apparent 10-11 days prior to onset. These anomalies: move the mid-Pacific jet axis southward, then extend the jet eastward (at about 35°N), narrow the latitude spread, and strengthen the jet stream over the eastern North Pacific. At onset, the positive zonal wind anomaly is strongly onshore, and the jet has a southwest orientation at the NorCal region, locally similar to but stronger than cluster 1.

In cluster 3 a tripolar zonal wind anomaly appears more than a week before onset. This tripolar pattern looks superficially similar to that in cluster 2 except with the opposite sign. A key difference is: the centers are roughly 25 degrees longitude further west. Starting about six days before onset, a dipole appears over western North America, including a positive westerly anomaly over NorCal. The main negative anomaly is centered on the climatological subtropical jet, causing it to broaden in latitude. As onset approaches, the two southern positive anomalies join, suggesting a flow from lower latitudes than the prior two clusters. The meridional wind component (supplemental material Fig. S1) has strong southerlies centered over Kamchatka and the NorCal region, with northerlies in between (Gulf of Alaska). So, the jet stream winds at NorCal are again southwesterly.

In cluster 4, longitudinally broad bands of zonal wind anomalies appear 5 days before onset. Westerlies are enhanced in the subtropics and over the Arctic Ocean. A large negative anomaly covers much of the middle latitudes, especially two days before onset. In the mid-Pacific, the climatological position of the subtropical jet is centered midway between the negative anomaly and the southern positive anomaly. The net effect of the anomalies is to build the subtropical jet on its equatorward side. Downwind the anomaly curls northward creating strong southwesterly flow at the NorCal region. (The meridional component is again strongly positive at the North American west coast.)

While the pattern of strong westerly flow (from a southwesterly orientation) at the NorCal region is *locally* very similar in all four clusters, how that local pattern is created differs greatly elsewhere, especially over the North Pacific.

3.2.3 Evolution of integrated vapor transport anomalies (IVTa)

Climatological total IVT has two major positive bands: eastward flux oriented WSW to ENE across the North Pacific (from 30-40°N) and a tropical band of westward IVT centered at 15°N in the western Pacific. There is a relative minimum along the Baja coast. Each cluster mean has strong onshore flow from the SW at NorCal. So, IVTa for each

cluster must be large over the NorCal region to overcome the climatological low IVT. Fig. 5 shows IVTa and 850 hPa horizontal wind anomaly vectors.

In cluster 1, a pair of zonal bands of positive IVTa form in the Pacific consistent with a positive streamfunction anomaly centered at 30°N. During the two days before PEx onset, the northern positive anomaly is driven towards the NorCal coast by the intensifying low pressure along the Canadian coast. This positive anomaly becomes confined close to the North American west coast and IVTa peaks over the NorCal region with a SW to NE orientation at onset. Negative IVTa covers a very large region northwest of NorCal, including all of Alaska. This large negative area is consistent with cold air advection as presumed from the northeasterly flow (850 hPa wind vectors). In turn, the cold advection supports the large negative 500 hPa streamfunction in Fig. 3.

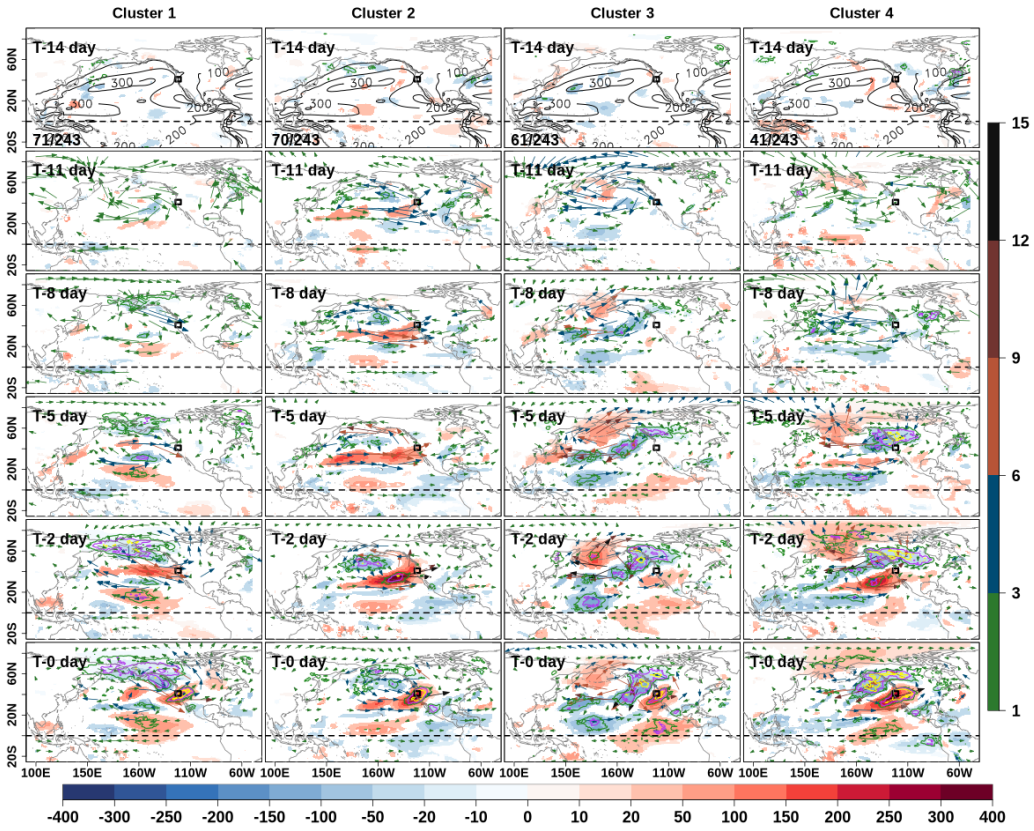

Figure 5: Same as Fig. 3 but for the evolution of integrated vapor transport (IVT) anomalies (shading; unit: kg/m-s). Solid black contours (contour interval: 100 kg/m-s in the top rows show the climatological total IVT. The vectors show the 850 hPa wind anomalies (unit: m/s). The bottom color bar pertains to the IVT anomalies, and the vertical color bar to the 850 hPa wind anomalies.

In cluster 2, a roughly zonal band of strongly positive IVTa develops along 35°N more than a week before the onset date, consistent with the cyclonic circulation visible in Fig. 3. This band looks similar to cluster 1 but its peak values are further east and moving more slowly during the two days before onset. The IVTa further intensifies and bends northeastward along the continental coast. Total IVT is shown in supplemental material Fig. S2. Similar to cluster 1, the moisture travels >70° longitude across the North Pacific. As with cluster 1, the *local* IVTa is again strongest and oriented SW-NE

over NorCal. There is negative IVTa northwest of the NorCal region but it is less extensive and south of the location in cluster 1. The associated northeasterly flow brings cold air off Alaska, supporting the negative streamfunction anomaly there.

Cluster 3 IVTa develops broad, significant, and consistent areas a week before onset. Somewhat opposite to cluster 2, a positive anomaly develops near the Aleutians. To the south and east a large negative anomaly forms, along 35-40°N arcing poleward into Canada. These two anomalies may be anticipated from flow around the equivalent-barotropic anomalies of $\Psi\mathbf{a}^{500}$ (and SLPa shown next). Unlike opposite-signed anomalies in cluster 2, these two anomalies stay in place, consistent with other variables, such as Fig. 3. Also consistent with prior figures, an intense positive IVTa develops close to the California coast (as well as a notable positive area in the tropics) only within two days before onset. Hence, while clusters 2 and 3 look like the "PNA" pattern shifted east and west respectively, positive IVTa at NorCal is present >5 days before onset in cluster 2, but only a day before onset in cluster 3. Also, while all clusters have positive IVTa at and adjacent to the CONUS coast, IVTa is negative to the west and southwest of that area in this cluster. In contrast with cluster 2, where a large positive IVTa anomaly travels eastward from beyond the dateline, the moisture source now is much closer to and southwest of NorCal, reflecting how this LSMP develops in place.

The moisture transport anomaly pattern in cluster 4 has similarities intermediate to those in clusters 2 and 3. Visible from day T-5 to onset, cluster 4 has a positive anomaly like cluster 2 that moves eastward several days before onset except is it now 5° further south. Cluster 4 is like cluster 3 in having a persistent negative anomaly where climatological IVT is the largest along the Canadian coast. Also like cluster 3, a large positive anomaly off Baja California occurs and extends across the equator. However, the enhanced transport crossing the California coast has its origin just north of Hawaii about 5 days before onset.

Notably, the local pattern of IVTa at onset is very similar in all clusters over the NorCal region: sign count locally largest and have a SW to NE orientation. As with other variables, the LSMP properties elsewhere differ markedly, especially 2 days before onset. Where cluster 2 and cluster 1 (a bit further north for the latter) have positive anomaly mid-Pacific, cluster 3 (and to some extent cluster 4) have negative anomaly there. Clusters 3 and 4 appear to have an obvious connection to subtropical latitudes while moisture transport in cluster 1 is more zonal at a much higher latitude. These differences between the patterns are less visible at the onset.

3.2.4 Evolution of sea level pressure anomalies (SLPa)

Fig. 6 shows *SLPa* evolution. The LSMPs are similar to Fig. 3 due to the equivalent-barotropic nature of the LSMPs. However, there are notable differences.

In cluster 1, a positive *SLPa* develops in the subtropical mid-Pacific around a week before the onset. This anomaly slowly expands eastward. A few days before onset, a low pressure anomaly over Alaska and western Canada forms in essentially the same location as at 500hPa. The low pressure anomaly moves southeastward to become 20° east of the 500 hPa location at onset. Southwesterly flow around that trough drives surface air onshore over NorCal.

The cluster 2 SLPa LSMP has a large low anomaly south of Alaska, much like the streamfunction anomaly in the mid and upper atmosphere. But unlike the upper air patterns (e.g. Fig. 3) the prominent high anomaly in the subtropics is missing. The negative SLPa low forms on the southeastern quadrant of the climatological atmospheric trough in the North Pacific. This low develops 11 days before onset. It subsequently strengthens and moves eastward until the anomaly is centered over the Canadian and NW USA west coast at onset, about 5° east of the 500hPa position. While cluster 1 has a simi-

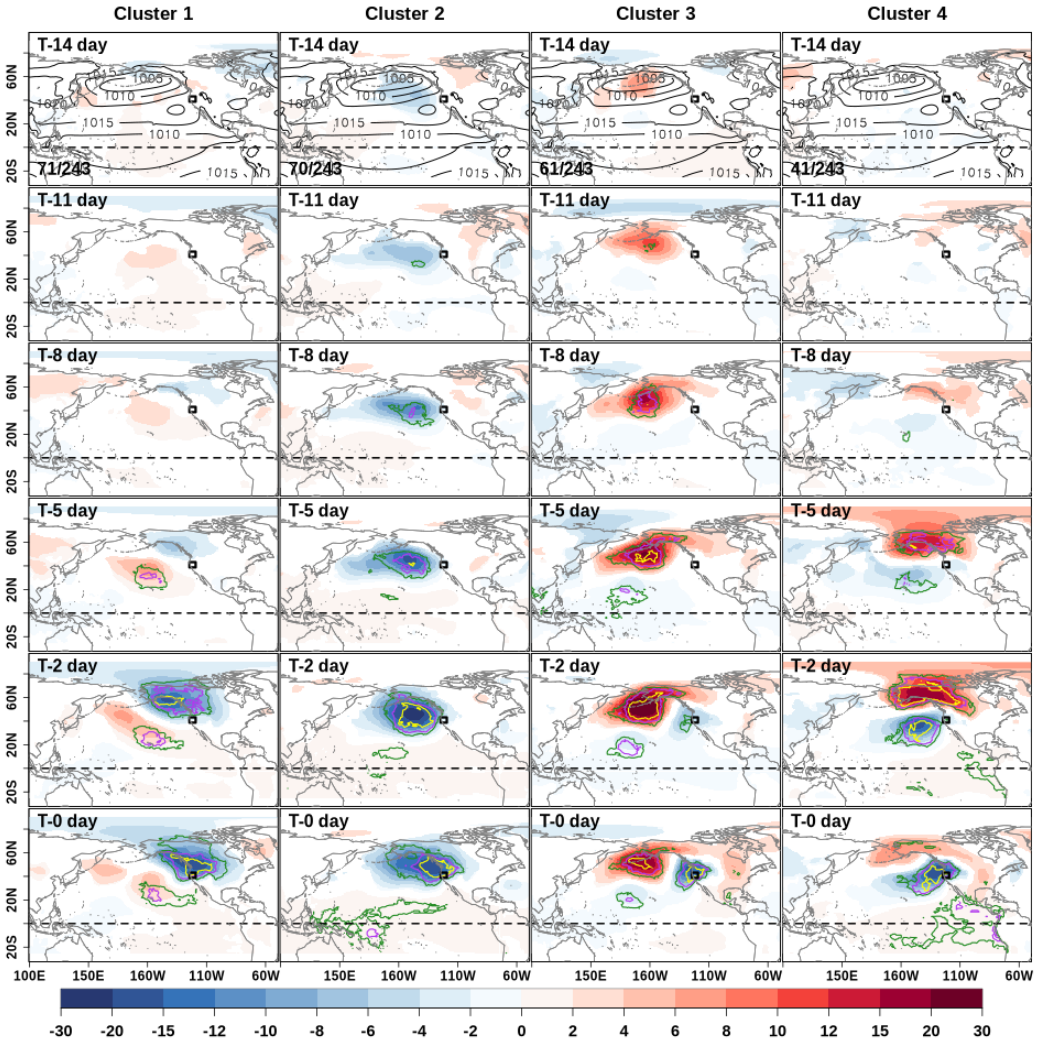

Figure 6: Same as Fig. 3 but for the evolution of sea level pressure anomaly (unit: hPa). Solid black contours (contour interval: 10 hPa) in the top rows show the climatological total sea level pressure.

lar low at onset, the time of formation is >10 days earlier and movement of the anomaly is eastward (instead of southeastward) for cluster 2. As with cluster 1, the anomaly fosters onshore surface flow over the NorCal region.

The cluster 3 LSMP is dominated by high SLPa centered just south of the Aleutians >10 days before onset. This anomaly is stationary, strengthens until day T-2 then wanes; it occurs through the depth of the troposphere. By day T-6, a stationary, weak low appears west of Hawaii, near the dateline, much weaker than its upper air counterpart. Only two days before onset the trough NW of NorCal appears, ∼5° SE of the upper troposphere trough. As in clusters 1 and 2, this anomaly would drive onshore surface winds, but this trough has a much smaller footprint. High SLP from the Great Lakes to Hudson Bay appears at onset; it is ∼10° east and much weaker than its upper air analog.

Cluster 4 has two dominant features. (i) A strong, large SLPa high over Alaska and NW Canada develops from day T-7 to day T-2, then diminishes by onset. (ii) A trough in the subtropical eastern Pacific strengthens as it moves northeastward from day T-5 to onset; it moves onshore ∼10° SE of the upper level trough at onset. This SLPa trough has a different orientation than other clusters in that it has a trailing portion extending SW into the subtropics. So, as with other variables, the pattern near the NorCal region at onset is similar in all four clusters, but elsewhere the patterns are quite different and especially strong at day T-2.

3.2.5 Evolution of 850hPa and other temperature anomalies

The evolution of the 850 hPa air temperature anomalies (Ta^{850}) for each of the four clusters is shown in Fig. 7. Climatologically, lower and middle tropospheric temperature contours are approximately zonally-oriented with deviations due to relatively warmer air off the west coast and colder air at the east coast of the continents. Higher up, at 200 hPa, the meridional temperature gradient is much weaker with cold anomalies centered over the NW US and central northern Asia regions (supplemental material Fig. S3). Ta^{850} is our archetype though the anomalies at other levels are plotted in the supplemental materials. Notably, the most prominent features in Ta^{200} generally have opposite sign, but similar location to the corresponding features in Ta^{850}. The evolution of skin temperature (SkT) differs from Ta^{850} by minimizing anomalies over the ocean. However, SkT has warm and cold anomalies over the tropical Pacific for clusters 2 and 3, respectively; but their possible links to ENSO are beyond the scope of this work.

Cluster 1 LSMP has three parts: 1) a warm anomaly largely confined to North America east of ∼120°E, 2) a cold anomaly from Alaska southeastward to just NW of NorCal, and 3) a mid-Pacific warm anomaly between 30-40°N. These three anomalies are present only two days before onset and occur throughout the troposphere. At 200 hPa (supplemental material Fig. S3) only a warm anomaly along the northern North America west coast is present; and as expected it has opposite sign to levels below (e.g. 500hPa, supplemental material Fig. S4). The primary cold anomaly near Alaska splits; the western portion remains over the Bering Sea while the eastern portion migrates along the Canadian west coast. Both motions can be anticipated from the expansion of the Aleutian low (e.g. Figs. 6 and 3) and advection by low level flow (e.g. supplemental material Fig. S2. The continental warm anomaly can be similarly explained by southwesterly flow over that broad region. The mid-Pacific anomaly is also consistent with low level southeasterly flow. Both warm anomalies create upper level height anomalies shown in Fig. 3.

Cluster 2 has two anomalies in the troposphere: a warm anomaly arcing from Hawaii across the western CONUS into central Canada and a cold anomaly to the west. The most consistent part of the cold anomaly travels eastward by 30-50° degrees longitude in the two days leading up to onset. The western part of the warm anomaly initially has two parts at T-5 days: a part over Alaska and a part in the mid to eastern subtropical

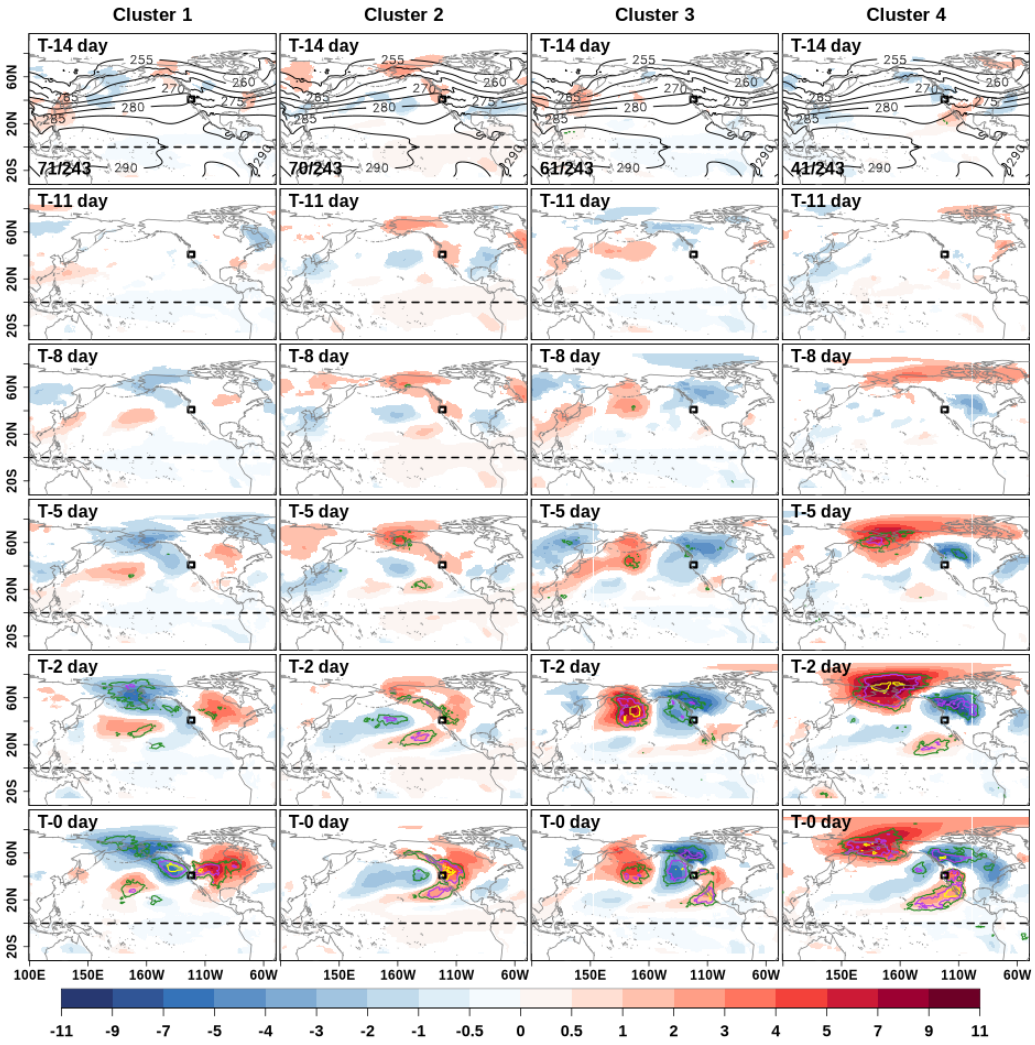

Figure 7: Same as Fig. 3 but for the evolution of the 850 hPa air temperature anomaly (unit: K). Solid black contours (contour interval: 5 K) in the top rows show the climatological 850 hPa air temperature.

Pacific centered at ∼60°N and ∼20°N, respectively. The northern warm anomaly moves eastward to form the aforementioned arc. Both warm anomalies merging to form an arc is largely explainable from advection around the huge primary tropospheric low pressure anomaly along with enhanced pressure closer to the equator, visible in Figs. 3 and 6. The subtropical warm anomaly from Hawaii eastward sits where westerly IVT, characteristic of the midlatitudes, is unusually far south (∼25°N) where other clusters have easterlies (clusters 1 and 3) or weak westerlies (cluster 4). This flow arises from the increased pressure gradient created by pressure and height anomalies that are: negative unusually far south but positive even further south, near 15-20°N, visible in previous figures. Skin temperatures (supplemental material Fig. S5) are also consistently warm there as well as along the equatorial Pacific from the dateline to Peru. Although it does not meet our consistency threshold (except a small area of Peru) the warm anomaly across the eastern equatorial Pacific is similar to the sea surface temperature pattern during an El Niño. Furthermore, the warm anomaly over the ocean along the west coast of North America that is accompanied by a cold anomaly in the central North Pacific resembles the positive phase of the Pacific decadal oscillation (PDO) pattern. Having this pattern, even though the ocean resists temperature changes, might suggest a preference for this cluster during positive PDO and El Nino. At 200 hPa a large warm anomaly is centered above the *cold* anomaly at 500 hPa.

In cluster 3, the 850 hPa temperature anomaly pattern has three parts that largely follow from flow around the two SLPa anomalies (Fig. 6). The west side of the huge pressure ridge drives subtropical air northward warming the northern Pacific and Bering Sea. Between that ridge and the low pressure at the NW CONUS cold air is driven southward from western Canada, across the Gulf of Alaska to southwest of NorCal. Finally, just prior to onset, a warm anomaly develops over Mexico. Unlike the prior two clusters, all three anomalies are essentially stationary over a week. This tri-polar temperature anomaly pattern generates three of the anomalies seen in 500hPa streamfunction shown in Fig. 3. The temperature anomalies at 500 hPa are similar to the lower elevation pattern except for a cold anomaly SW of Hawaii that matches 500hPa patterns in Figs. 2 and 3. The skin temperature (supplemental material Fig. S5) is somewhat similar to 850 hPa over the land masses but also has some notable oceanic anomalies: an intense warm anomaly south of the Aleutians and an equatorial eastern Pacific cold anomaly. The latter is suggestive of "La Niña" conditions. At 200 hPa, the anomalies are opposite-signed and largely coincident to those at 850 hPa, but with the addition of a warm anomaly above eastern Siberia. A difference from other levels is the Aleutian and Mexican cold anomalies are connected at 200hPa. Of the levels discussed, these anomalies are most prominent at 500hPa, where they appear a week before onset.

The key characteristic in cluster 4 in Fig. 7 is the deep, stationary, warm anomaly covering Alaska, Bering Sea, and much of the Arctic Ocean. The broad extent invites comparison with future climate simulations showing amplified Arctic warming, thereby suggesting that this cluster may become more common in the future. This anomaly is also quite strong at 500hPa and consistent with low-level flow implied by SLPa. Over western Canada, an intense cold anomaly in Ta^{850} (and SkT) develops a few days before onset. At 500 hPa, this cold anomaly is less prominent (supplemental material Fig. S4). Also developing shortly before onset is a highly consistent warm anomaly extending from the PEx area southwestward into the subtropical Pacific as far as Hawaii. South of 40°N, this latter warm anomaly has similar extent to cluster 2, except it is slightly further south over the ocean. Unlike cluster 2, this more southern warm anomaly only develops just before onset. The 200 hPa pattern (supplemental material Fig. S3) has a cold anomaly above Alaska and the adjacent ocean nearly a week before onset followed by a warm anomaly to the south that intensifies and rotates to the Canadian west coast at onset. Those two anomalies are explainable from the 200 hPa streamfunction, which has a positive anomaly between them and a negative anomaly to the west of them: the resultant flow creates these 200 hPa temperature anomalies from thermal advection. The

Ta^{850}, Ta^{500}, and SkT patterns north of ∼45°N are strongest at T-2 and largely opposite-signed from cluster 1, though close to the PEx region at onset their temperature anomalies match.

3.3 Probabalistic predictions of precipitation extremes using LSMPi as predictors

This subsection shows some tests using individual LSMPi values, both at and prior to onset, to predict heavy precipitation values. As described in section 2.2, we construct LSMPs from two periods of data: training LSMPs $\overline{LY}_{l*}^{c,T}$ and verification LSMPs $\overline{LY}_{l*}^{c,V}$ and do so for 0-6 days prior to onset. The training period is 1948-1982, while the verification period is 1982-2015; both periods use NDJFM months. We find that the LSMP clusters in the training and verification data are similar in spatial pattern, significance and consistency, an example of which is shown in supplemental material Fig. S6. The strong resemblance between the training and verification LSMPs supports the robustness of the *patterns* irrespective of the different training and verification periods. Less important to the discussion here is that we find more variation in the *frequency* of each cluster type. The numbers in clusters 1 and 2 are similar in both periods, but there are fewer members in clusters 3 and 4 in the verification period. We do not explore climate change issues in this report.

As described in section 2.3, we constructed training and verification LSMPis from daily anomalies of the atmospheric variables that show large-scale synoptic patterns prior to the PEx onset. The tested variables are anomalies of 500hPa geopotential height (Za^{500}), 500 and 850 hPa air temperatures (Ta^{500} and Ta^{850}), 850 hPa zonal and meridional winds (Ua^{850} and Va^{850}), sea level pressure ($SLPa$), skin temperature (Ts), precipitable water (PWa) and $IVTa$. Our discussion of relative skill emphasizes metrics designed for binary predictions. While statistically valid, such measures are not ideal for this problem because near misses are not distinguished from large misses. As noted in Grotjahn (2011) there is more forecast value in near misses than large misses.

Supplemental materials Table S1 shows measures of prediction skills when using LSMPis as predictors of extreme precipitation at lag 0 (and lag 2, in parenthesis). It is apparent that for all these variables, hits exceed misses by a large margin, indicating that the LSMPis can capture occurrences of PEx events very well. Of course, the skill decreases as the lag increases. But the LSMPi do so well that even at two days lag; they forecast the event occurrence with high accuracy. For all the variables, the probability of detection (POD) at lag 0 is 0.74 or more (0.52 at lag 2). The maximum POD is offered by IVT at lags 0 (0.89 for training and 0.78 for verification data). Notably, the false alarm ratio ($FAR = FA/(hits + FA)$) is comparable to the POD for each variable. However, assessing the forecast skill by comparing POD with FAR may be misleading because the predictands (extreme precipitation events) are rare by definition (occurring less than 5% of the time). As explained in Ebert and Milne (2022), the evaluation of forecast skill based upon proportion-correct measures is not appropriate for predicting rare events. The TS and GSS scores are much lower than the PSS values for each variable. Ebert and Milne (2022) highlight the discrepancy among different skill scores when making forecasts for rare events. They suggest that the Pierce skill score is the only skill score that meets all three adequacy constraints for a proper measure of skill in rare events. Also notable is that the forecast skills for training and verification data are comparable, and there is no drastic fall in forecast skills when LSMPi is constructed by projecting the training LSMPs (constructed for the period NDJFM of 1948-1982) onto the daily meteorological fields over an independent (verification) period (NDJFM of 1982-2015). IVT is superior in each of the metrics, which is perhaps unsurprising given that all the LSMPs show an atmospheric river-like pattern over the PEx Region. Similarly, other studies of the circulation close to the PEx region have strong IVT around the south side of a trough that is unusually far south (e.g., Grotjahn & Faure, 2008; D. Chen et al., 2021).

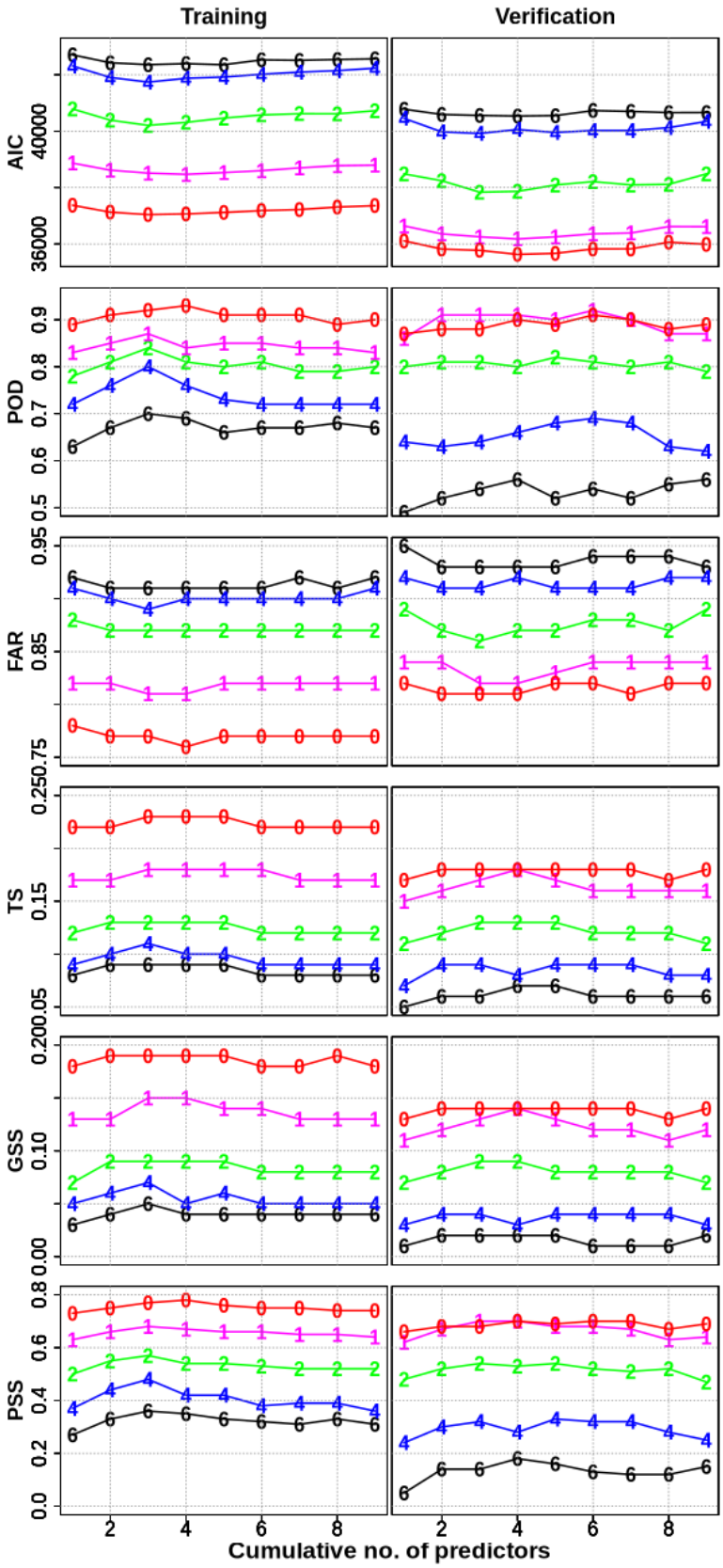

Figure 8: Prediction skill measures for combinations of LSMPi predictors. The x-axis shows the cumulative number of predictors while the individual lines are for lags 0, 1, 2, 4, and 6. The LSMPi predictors (LSMPis) are combined using the order as shown in Table 2. Training period: 1948-1982 ; verification period: 1982-2015.

Table 2: Cumulative ordering of variables (LSMPis) according to their fitness as predictors of the PEx events at different lags in the training dataset. The predictors are added cumulatively. The ordering shows the best predictor (or predictor combination), based on AIC, each time a set of predictors is tested. Refer to the text for more details. The variables shown are anomalies but the subscript 'a' has been removed for brevity here.

Cumulative ordering based on AIC	lag6	lag4	lag2	lag1	lag0
1	PW	PW	IVT	IVT	IVT
2	SLP	U850	PW	SLP	U850
3	IVT	V850	U850	PW	PW
4	U850	IVT	V850	U850	SLP
5	T850	SLP	SLP	V850	V850
6	V850	T850	T500	Z500	Z500
7	T500	Z500	Z500	Ts	T500
8	T500	T500	Ts	T500	T850
9	Ts	Ts	T850	T850	Ts

Table S1 includes the Akaike Information criteria (AIC), which is a measure of the fitness of a variable as a predictor of PEx events. When comparing two variables, a variable with a lower AIC is considered a better predictor. Table 2 indicates that the most skillful predictive combination of variables varies with lag. For example, for lag 0, IVT is the best single predictor, then the best combination for two predictors is IVT with U850. For three and four predictors, add PW then SLP in the training dataset. However, for lag 2, prediction is best when IVT is followed by PW (and then U850) when two (and then three) predictors are used, respectively, in the training dataset. Hence, IVT+U850+PW is the best combination of three variables at lag 0. These optimal combinations of predictor variables, shown in Table 2, indicate that the best combination of predictors varies with lag time. That is, the set of predictor variables giving the best prediction of PEx events varies with the lag. How many predictor variables together can best predict the PEx events based on our binary metrics? Fig. 8 shows prediction skill metrics in the training and verification time periods for different numbers of predictor variables at lags 0-6. The same combinations of predictor variables (Table 2) are used for predicting PEx events in the training and verification time periods. The criteria of the fitness of predictors, AIC, shows that for shorter lead times (0-2 days), AIC is minimum for a combination of 3-4 predictor variables, suggesting that the combination of 3-4 of our predictor variables fits the prediction model best, and adding any more variable either adds no further improvement or possibly degrades the prediction. For longer lead time (4-6 days), AIC varies little with the number of predictors, though some other metrics do best with at least 3 or 4 predictors. The forecast skill based upon PSS suggests that the forecast skill is best for a combination of 3 to 4 variables for lags 1-6. But, there is little improvement in prediction skills when using more than one predictor for lag 0 in the verification data. A comparison of the left and right columns in Fig. 8 suggests that the fitness of predictor variables degrades a bit when the combination of predictor variables based upon training data is used to predict PEx events in the verification set. Similarly, the prediction skills are slightly degraded for verification data. However, there is no drastic fall in prediction skill (PSS) when compared with the training data. Moisture-based variables such as IVT or PW are the best predictors at any lag. Also, lower-level atmospheric variables (e.g., U850) are better predictors than mid-level atmospheric variables (e.g., T500). Most notably, IVT is the best predictor until 2 days before the onset but

is the third best predictor nearly a week before the onset (lag 6). This analysis suggests that LSMPs do offer predictability of PEx events, but one must select the suitable variable depending on how far in advance one wants to make a prediction.

Fig. 9(a) shows the probabilistic prediction of precipitation using IVT LSMPi as a predictor of PEx in the training dataset. The IVT LSMPi and PEx have a significant (at the 5% level) correlation of 0.43 based on Spearman's rank correlation test. Out of the 23 copulas tested, we find that the Joe copula performs the best based on maximum likelihood estimates. Therefore, we use the Joe copula to make predictions of the precipitation values. In the figure, the vertical color bars show the likelihood of predicted values, so the yellows indicate low likelihood, and blues indicate a high likelihood of the predicted precipitation values. The figure shows that LSMPi constructed from IVT can predict the observed precipitation values (red dots) with high likelihood as most of the observed precipitation values are within the highly likely region (likelihood ≥ 0.75). The uncertainties in these predictions are shown by the black dots, which show the 95% confidence interval of the predicted values. Almost all of the observed extreme precipitation values lie within the 95% confidence interval. Fig. 9(b) shows the predictions of PEx events based on the verification data. As might be expected from the previous figure, the predictions in the verification data are not quite as good as in the training data, but they remain comparable to those in the training data. This analysis shows that the LSMPis are skillful predictors of extreme precipitation values when evaluated on independent data.

4 Discussion and Conclusions

Previous studies show that there is more than one set of large-scale circulation patterns that create extreme precipitation (PEx) events over Northern California (NorCal). In some of the published works, the large-scale circulation patterns connected to PEx events (or any other extreme meteorological events) are loosely described as *Large Scale Meteorological Patterns* (LSMPs). However, a true LSMP, as defined by Grotjahn (2011), is more than a simple composite or aggregate, and it must indicate what is *important* in that composite or aggregate. What is important must pass both a significance test *and* a consistency test (like sign counts). To emphasize these statistical tests, we rename "LSMP" to be large-scale statistically meaningful patterns, here associated with PEx over NorCal. These have been our broad objectives: First, we establish what the minimum number of LSMP clusters are for NorCal PEx events. Second, we identify what is consistent and significant in the LSMP clusters of meteorological variables leading to PEx events. Third, we present a framework for the probabilistic predictions of PEx events using LSMP-based indices (LSMPis) as predictors. Those aspects of the current study have never been examined before.

We identified 311 PEx events, defined as the 24-hr precipitation averaged over the NorCal region ($\overline{P}$) greater than the 95^{th} percentile of $\overline{P}$ over the 1948-2015 period from the CPC data. We apply k-means clustering analysis to the first two principal components of 500hPa geopotential height anomalies (Za^{500}_{I2}) two days before the 311 PEx onset dates. The patterns are most strongly distinguishable two days before onset and that is why we chose that timeframe for the clustering. Our analysis, using both the statistical and heuristic methods, suggests that a minimum of four clusters can explain NorCal PEx events. To analyze clusters whose members are distinct from members in other clusters, we removed PEx events identified as "mixed cases". This procedure reduces the number of PEx events to 243. The four clusters are identified as 1) *northwestern continental negative height anomaly* that has a large negative geopotential height anomaly extending over Alaska, western Canada, and the the NW CONUS, 2) *eastward positive "PNA"* that has a large negative Za^{500} centered over the northern Pacific co-existing with a positive Za^{500} to the south of it over the central tropical Pacific (between 20°N and 20°S) and a wavetrain to the east, 3) *westward negative "PNA"* pattern having a very strong positive Za^{500} centered over the Aleutian region with low heights to the south

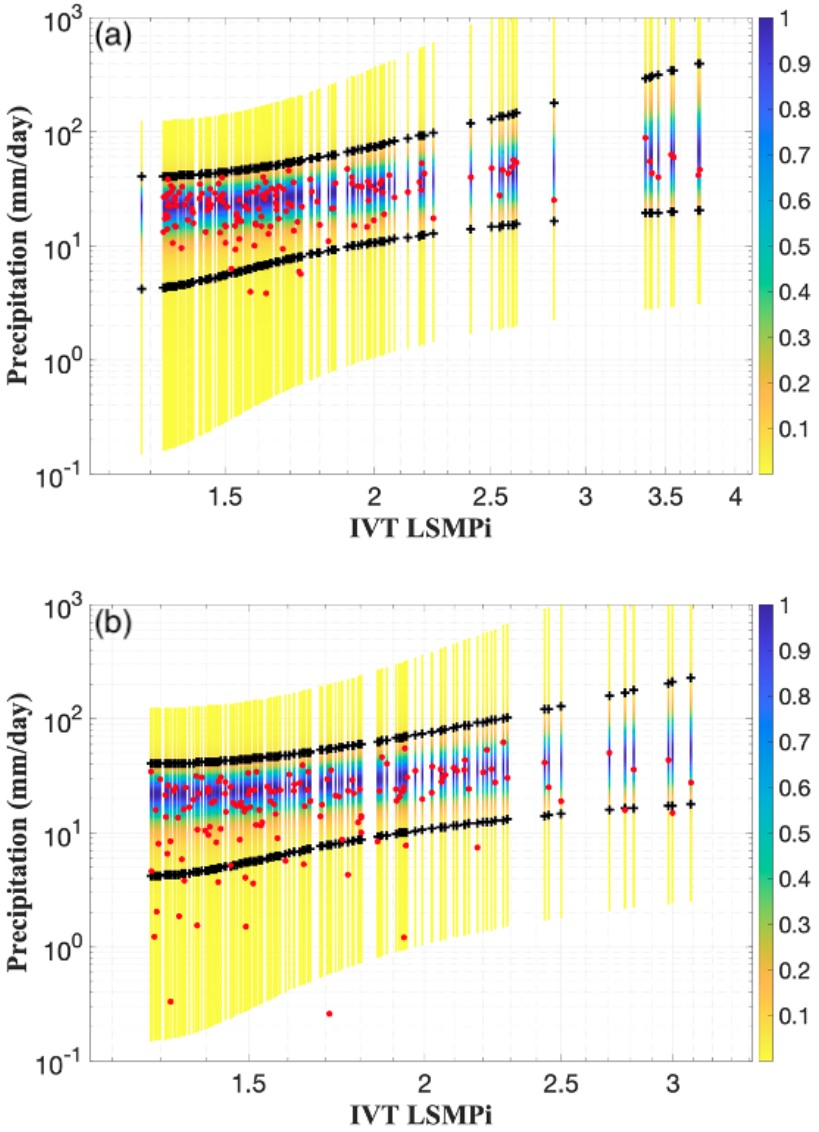

Figure 9: Probabilistic prediction of the precipitation amount (mm/day) using a single LSMP index (LSMPi) as a test. This test uses lag 2 data. Precipitation values are shown (red dots) for each day that the IVT LSMPi value exceeds its 95% in the training (a) and verification data (b). The black dots mark the 95% range of predicted precipitation for that LSMPi value. The Y-axis uses a log-scale. The methods section provides details.

over the subtropical Pacific and a wavetrain to the east that creates a strong Za^{500} near the Canadian west coast. 4) *Prominent Alaskan ridge* that has a prominent positive Za^{500} over Alaska and the adjacent Arctic Ocean with a trough across the midlatitude Pacific arcing into the NW CONUS.

The investigation of synoptic properties leading to PEx onset suggests that the LSMPs evolve differently from each other. The LSMP patterns near NorCal are essentially the same at PEx onset, but they have distinctly different patterns further away from the NorCal region and leading up to onset. For example, as the names of the clusters suggest, the streamfunction (and geopotential) anomalies have distinct spatial signatures in all four clusters. Also, in two clusters a prominent part of the LSMP is present at least a week before onset while other clusters develop their LSMPs only a couple days before onset. Some clusters have nearly stationary anomalies that form the low pressure NW of NorCal while other clusters have multiple features that travel large horizontal distances. The source of the moisture varies: from west of the dateline in the midlatitude Pacific, to ocean >30° west of NorCal, to the tropical Pacific near Hawaii, and in between. Though IVT anomalies (IVTa) at the onset have the same southwestern to northeastern orientation near NorCal for all clusters, cluster 2 and cluster 1 have positive IVTa mid-Pacific, while clusters 3 and 4 have negative IVTa there. Cluster 4 has a distinct stationary, warm lower tropospheric temperature anomaly over Alaska and much of the Arctic Ocean, in contrast, cluster 1 has a cold anomaly over the northeastern Pacific and Alaska that develops by onset. We find evidence that the NorCal PEx events have tropical connections, such as significant and consistent Za^{500} south of 20°N crossing the equator. Significant but not sufficiently consistent skin temperature anomalies hint at possible El Niño and La Niña influences on PEx events in clusters 2 and 3, respectively.

We estimated the predictive skills of LSMPis constructed from the training and verification periods. We constructed the LSMPi for a variable in the training and verification data by projecting the *training* LSMP onto the related daily variable in the training and verification data, respectively. Simple binary forecast metrics (e.g., POD, FAR, PSS) show that the LSMPis have skill both capturing onset PEx as well as predicting PEx several days in advance. The best predictor tested was moisture-based with IVT being superior a day or two before onset. Also, lower-level variables we tested have superior prediction skill compared to middle or upper levels, at least up to 6 days before the onset. We tested the concept of using LSMPis to make probabilistic predictions of the amount of precipitation and found even one predictor has skill.

This LSMP-based work provides a useful framework for the process-based evaluation of climate models by climate scientists and practitioners (e.g., water managers). Since LSMPs are synoptic-scale patterns, they can be detected in coarse-resolution climate models. The LSMP patterns identified in this work can be used to evaluate climate models for applications such as model selection and weighting for future projections by stakeholders and scientists.

Our work prompts further research. For example, as discussed in Reed et al. (2022) and shown by Palipane and Grotjahn (2018), LSMPs provide a useful metric for evaluating model skill. Our work suggests tropical teleconnections to the NorCal PEx events that could be further explored. We demonstrated that probabilistic prediction is feasible with LSMPis and the use of multiple LSMPis should be explored to improve such prediction, based on qualitative results in (Grotjahn, 2011). Decadal average precipitation slowly declines over NorCal during our study period but the number of PEx events first declines by half before rebounding over the decades, the fractions of PEx events by each cluster varies greatly, too; we hope to report on these trends in a future publication. Potential future work could use the LSMP-based framework for model skill evaluations over the NorCal region, investigating changes in LSMPs in response to global warming, understanding the tropical impact on the NorCal PEx events, and designing storyline-based simulations to understand the effect of climate change on the historical

large flood events over California (e.g., Rhoades et al., 2023). LSMPs in other time frames could be examined: Moore et al. (2021) find similar aggregates (not LSMPs) for 5-day averages that look similar to the LSMPs we show for 24-hour average PEx. LSMP analyses for PEx in other contexts could be explored such as rain versus snow-producing events. Finally, most of these questions could be explored for other regions of Earth.

Open Research

CPC Unified Gauge-Based Analysis of Daily Precipitation over CONUS data provided by the NOAA PSL, Boulder, Colorado, USA, from their website at `https://psl.noaa.gov`. Support for the Twentieth Century Reanalysis Project version 3 dataset is provided by the U.S. Department of Energy, Office of Science Biological and Environmental Research (BER), by the National Oceanic and Atmospheric Administration Climate Program Office, and by the NOAA Physical Sciences Laboratory.

Acknowledgments
This work is supported by the Department of Energy Office of Science award numbers DE-SC0016605, "A Framework for Improving Analysis and Modeling of Earth System and Intersectoral Dynamics at Regional Scales" and DE-AC02-05CH11231 for the CASCADE Scientific Focus (funded by the Regional and Global Model Analysis Program area within the Earth and Environmental Systems Modeling Program). We sincerely thank Prof. Mojtaba Sadegh, Boise State University, Boise, ID, USA, for his valuable suggestions and MATLAB code for the copula analysis. We also thank Prof. David Straus, George Mason University, Fairfax, VA, USA, for his guidance on the clustering analysis.

The authors declare that they have no conflict of interest.

References

Agel, L., & Barlow, M. (2020). How well do cmip6 historical runs match observed northeast u.s. precipitation and extreme precipitation–related circulation? *Journal of Climate*, *33*(22), 9835 - 9848. Retrieved from `https://journals.ametsoc.org/view/journals/clim/33/22/jcliD191025.xml` doi: https://doi.org/10.1175/JCLI-D-19-1025.1

Agel, L., Barlow, M., Feldstein, S. B., & Gutowski, W. J. (2018). Identification of large-scale meteorological patterns associated with extreme precipitation in the us northeast. *Climate dynamics*, *50*, 1819–1839.

AghaKouchak, A., Bárdossy, A., & Habib, E. (2010). Copula-based uncertainty modelling: application to multisensor precipitation estimates. *Hydrological Processes*, *24*(15), 2111-2124. Retrieved from `https://onlinelibrary.wiley.com/doi/abs/10.1002/hyp.7632` doi: https://doi.org/10.1002/hyp.7632

Akaike, H. (1974, December). A new look at the statistical model identification. *IEEE Transactions on Automatic Control*, *19*(6), 716-723. doi: 10.1109/TAC.1974.1100705

Amini, S., & Straus, D. M. (2019). Control of storminess over the pacific and north america by circulation regimes: The role of large-scale dynamics in weather extremes. *Climate Dynamics*, *52*(7-8), 4749–4770. doi: https://doi.org/10.1007/s00382-018-4409-7

Barlow, M., Gutowski, W. J., Gyakum, J. R., Katz, R. W., Lim, Y.-K., Schumacher, R. S., ... others (2019). North american extreme precipitation events and related large-scale meteorological patterns: a review of statistical methods, dynamics, modeling, and trends. *Climate Dynamics*, *53*, 6835–6875. doi: https://doi.org/10.1007/s00382-019-04958-z

Barnston, A. G., & Livezey, R. E. (1987). Classification, seasonality and persistence of low-frequency atmospheric circulation patterns. *Monthly Weather Review*, *115*(6), 1083 - 1126. Retrieved from `https://journals.ametsoc.org/view/journals/mwre/115/6/1520-0493_1987_115_1083_csapol_2_0_co_2.xml` doi: 10.1175/1520-0493(1987)115⟨1083:CSAPOL⟩2.0.CO;2

Boroneant, C., Plaut, G., Giorgi, F., & Bi, X. (2006). Extreme precipitation over the maritime alps and associated weather regimes simulated by a regional climate model: Present-day and future climate scenarios. *Theoretical and Applied Climatology*, *86*, 81–99.

Chen, D., Norris, J., Goldenson, N., Thackeray, C., & Hall, A. (2021). A distinct atmospheric mode for california precipitation. *Journal of Geophysical Research: Atmospheres*, *126*(12), e2020JD034403. Retrieved from `https://agupubs.onlinelibrary.wiley.com/doi/abs/10.1029/2020JD034403` (e2020JD034403 2020JD034403) doi: https://doi.org/10.1029/2020JD034403

Chen, M., Shi, W., Xie, P., Silva, V. B. S., Kousky, V. E., Wayne, H. R., & Janowiak, J. E. (2008). Assessing objective techniques for gauge-based analyses of global daily precipitation. *Journal of Geophysical Research: Atmospheres*, *113*(D4). Retrieved from `https://agupubs.onlinelibrary.wiley.com/doi/abs/10.1029/2007JD009132` doi: https://doi.org/10.1029/2007JD009132

Collow, A. B. M., Bosilovich, M. G., & Koster, R. D. (2016). Large-scale influences on summertime extreme precipitation in the northeastern united states. *Journal of Hydrometeorology*, *17*(12), 3045 - 3061. Retrieved from `https://journals.ametsoc.org/view/journals/hydr/17/12/jhm-d-16-0091_1.xml` doi: https://doi.org/10.1175/JHM-D-16-0091.1

Collow, A. B. M., Mersiovsky, H., & Bosilovich, M. G. (2020). Large-scale influences on atmospheric river–induced extreme precipitation events along the coast of washington state. *Journal of Hydrometeorology*, *21*(9), 2139 - 2156. Retrieved from `https://journals.ametsoc.org/view/journals/hydr/21/9/jhmD190272.xml` doi: https://doi.org/10.1175/JHM-D-19-0272.1

DeAngelis, A. M., Broccoli, A. J., & Decker, S. G. (2013). A comparison of cmip3 simulations of precipitation over north america with observations: Daily statistics and circulation features accompanying extreme events. *Journal of Climate*, *26*(10), 3209 - 3230. Retrieved from https://journals.ametsoc.org/view/journals/clim/26/10/jcli-d-12-00374.1.xml doi: https://doi.org/10.1175/JCLI-D-12-00374.1

Dettinger, M. D., Ralph, F. M., Das, T., Neiman, P. J., & Cayan, D. R. (2011). Atmospheric rivers, floods and the water resources of california. *Water*, *3*(2), 445–478. Retrieved from https://www.mdpi.com/2073-4441/3/2/445 doi: 10.3390/w3020445

Ebert, P. A., & Milne, P. (2022). Methodological and conceptual challenges in rare and severe event forecast verification. *Natural Hazards and Earth System Sciences*, *22*(2), 539–557. Retrieved from https://nhess.copernicus.org/articles/22/539/2022/ doi: 10.5194/nhess-22-539-2022

Gao, X., & Mathur, S. (2021). Predictability of u.s. regional extreme precipitation occurrence based on large-scale meteorological patterns (lsmps). *Journal of Climate*, *34*(17), 7181 - 7198. Retrieved from https://journals.ametsoc.org/view/journals/clim/34/17/JCLI-D-21-0137.1.xml doi: https://doi.org/10.1175/JCLI-D-21-0137.1

Gao, X., Schlosser, C. A., Xie, P., Monier, E., & Entekhabi, D. (2014). An analogue approach to identify heavy precipitation events: Evaluation and application to cmip5 climate models in the united states. *Journal of Climate*, *27*(15), 5941 - 5963. Retrieved from https://journals.ametsoc.org/view/journals/clim/27/15/jcli-d-13-00598.1.xml doi: https://doi.org/10.1175/JCLI-D-13-00598.1

Gershunov, A., Shulgina, T., Ralph, F. M., Lavers, D. A., & Rutz, J. J. (2017). Assessing the climate-scale variability of atmospheric rivers affecting western north america. *Geophysical Research Letters*, *44*(15), 7900-7908. Retrieved from https://agupubs.onlinelibrary.wiley.com/doi/abs/10.1002/2017GL074175 doi: https://doi.org/10.1002/2017GL074175

Grotjahn, R. (2011). Identifying extreme hottest days from large scale upper air data: a pilot scheme to find california central valley summertime maximum surface temperatures. *Climate dynamics*, *37*, 587–604. doi: https://doi.org/10.1007/s00382-011-0999-z

Grotjahn, R., Black, R., Leung, R., Wehner, M. F., Barlow, M., Bosilovich, M., ... others (2016). North american extreme temperature events and related large scale meteorological patterns: a review of statistical methods, dynamics, modeling, and trends. *Climate Dynamics*, *46*, 1151–1184. doi: https://doi.org/10.1007/s00382-015-2638-6

Grotjahn, R., & Faure, G. (2008). Composite predictor maps of extraordinary weather events in the sacramento, california, region. *Weather and Forecasting*, *23*(3), 313 - 335. Retrieved from https://journals.ametsoc.org/view/journals/wefo/23/3/2007waf2006055_1.xml doi: https://doi.org/10.1175/2007WAF2006055.1

Grotjahn, R., & Zhang, R. (2017). Synoptic analysis of cold air outbreaks over the california central valley. *Journal of Climate*, *30*(23), 9417 - 9433. Retrieved from https://journals.ametsoc.org/view/journals/clim/30/23/jcli-d-17-0167.1.xml doi: https://doi.org/10.1175/JCLI-D-17-0167.1

Guirguis, K., Gershunov, A., Clemesha, R. E. S., Shulgina, T., Subramanian, A. C., & Ralph, F. M. (2018). Circulation drivers of atmospheric rivers at the north american west coast. *Geophysical Research Letters*, *45*(22), 12,576-12,584. Retrieved from https://agupubs.onlinelibrary.wiley.com/doi/abs/10.1029/2018GL079249 doi: https://doi.org/10.1029/2018GL079249

Guirguis, K., Gershunov, A., DeFlorio, M. J., Shulgina, T., Delle Monache, L., Subramanian, A. C., ... Ralph, F. M. (2020). Four atmospheric circulation

regimes over the north pacific and their relationship to california precipitation on daily to seasonal timescales. *Geophysical Research Letters*, *47*(16), e2020GL087609. Retrieved from https://agupubs.onlinelibrary.wiley.com/doi/abs/10.1029/2020GL087609 (e2020GL087609 2020GL087609) doi: https://doi.org/10.1029/2020GL087609

Guirguis, K., Gershunov, A., Shulgina, T., Clemesha, R. E., & Ralph, F. M. (2019). Atmospheric rivers impacting northern california and their modulation by a variable climate. *Climate Dynamics*, *52*, 6569–6583. doi: https://doi.org/10.1007/s00382-018-4532-5

Gutowski, W. J., Decker, S. G., Donavon, R. A., Pan, Z., Arritt, R. W., & Takle, E. S. (2003). Temporal–spatial scales of observed and simulated precipitation in central u.s. climate. *Journal of Climate*, *16*(22), 3841 - 3847. Retrieved from https://journals.ametsoc.org/view/journals/clim/16/22/1520-0442_2003_016_3841_tsooas_2.0.co_2.xml doi: https://doi.org/10.1175/1520-0442(2003)016⟨3841:TSOOAS⟩2.0.CO;2

Hao, Z., & AghaKouchak, A. (2013). Multivariate standardized drought index: A parametric multi-index model. *Advances in Water Resources*, *57*, 12-18. Retrieved from https://www.sciencedirect.com/science/article/pii/S0309170813000493 doi: https://doi.org/10.1016/j.advwatres.2013.03.009

Leathers, D. J., Yarnal, B., & Palecki, M. A. (1991). The pacific/north american teleconnection pattern and united states climate. part i: Regional temperature and precipitation associations. *Journal of Climate*, *4*(5), 517 - 528. Retrieved from https://journals.ametsoc.org/view/journals/clim/4/5/1520-0442_1991_004_0517_tpatpa_2_0_co_2.xml doi: 10.1175/1520-0442(1991)004⟨0517:TPATPA⟩2.0.CO;2

Lee, Y.-Y., & Grotjahn, R. (2016). California central valley summer heat waves form two ways. *Journal of Climate*, *29*, 1201-1217. Retrieved from https://doi.org/10.1175/JCLI-D-15-0270.1

Loikith, P. C., Lintner, B. R., & Sweeney, A. (2017). Characterizing large-scale meteorological patterns and associated temperature and precipitation extremes over the northwestern united states using self-organizing maps. *Journal of Climate*, *30*(8), 2829 - 2847. Retrieved from https://journals.ametsoc.org/view/journals/clim/30/8/jcli-d-16-0670.1.xml doi: https://doi.org/10.1175/JCLI-D-16-0670.1

Moore, B. J., White, A. B., & Gottas, D. J. (2021). Characteristics of long-duration heavy precipitation events along the west coast of the united states. *Monthly Weather Review*, *149*(7), 2255 - 2277. Retrieved from https://journals.ametsoc.org/view/journals/mwre/149/7/MWR-D-20-0336.1.xml doi: https://doi.org/10.1175/MWR-D-20-0336.1

Moore, B. J., White, A. B., Gottas, D. J., & Neiman, P. J. (2020). Extreme precipitation events in northern california during winter 2016–17: Multiscale analysis and climatological perspective. *Monthly Weather Review*, *148*(3), 1049 - 1074. Retrieved from https://journals.ametsoc.org/view/journals/mwre/148/3/mwr-d-19-0242.1.xml doi: https://doi.org/10.1175/MWR-D-19-0242.1

Neiman, P. J., Ralph, F. M., White, A. B., Kingsmill, D. E., & Persson, P. O. G. (2002). The statistical relationship between upslope flow and rainfall in california's coastal mountains: Observations during caljet. *Monthly Weather Review*, *130*(6), 1468 - 1492. Retrieved from https://journals.ametsoc.org/view/journals/mwre/130/6/1520-0493_2002_130_1468_tsrbuf_2.0.co_2.xml doi: https://doi.org/10.1175/1520-0493(2002)130⟨1468:TSRBUF⟩2.0.CO;2

Neiman, P. J., Ralph, F. M., Wick, G. A., Lundquist, J. D., & Dettinger, M. D. (2008). Meteorological characteristics and overland precipitation impacts of atmospheric rivers affecting the west coast of north america based on eight years of ssm/i satellite observations. *Journal of Hydrometeorology*, *9*(1), 22 - 47. Retrieved from https://journals.ametsoc.org/view/journals/hydr/9/

1/2007jhm855_1.xml doi: https://doi.org/10.1175/2007JHM855.1

Palipane, E., & Grotjahn, R. (2018). Future projections of the large-scale meteorology associated with california heat waves in cmip5 models. *Journal of Geophysical Research: Atmospheres*, *123*(16), 8500-8517. Retrieved from https://agupubs.onlinelibrary.wiley.com/doi/abs/10.1029/2018JD029000 doi: https://doi.org/10.1029/2018JD029000

Payne, A. E., & Magnusdottir, G. (2014). Dynamics of landfalling atmospheric rivers over the north pacific in 30 years of merra reanalysis. *Journal of Climate*, *27*(18), 7133 - 7150. Retrieved from https://journals.ametsoc.org/view/journals/clim/27/18/jcli-d-14-00034.1.xml doi: https://doi.org/10.1175/JCLI-D-14-00034.1

Polade, S. D., Gershunov, A., Cayan, D. R., Dettinger, M. D., & Pierce, D. W. (2017). Precipitation in a warming world: Assessing projected hydro-climate changes in california and other mediterranean climate regions. *Scientific reports*, *7*(1), 10783. doi: https://doi.org/10.1038/s41598-017-11285-y

Ralph, F. M., Neiman, P. J., Wick, G. A., Gutman, S. I., Dettinger, M. D., Cayan, D. R., & White, A. B. (2006). Flooding on california's russian river: Role of atmospheric rivers. *Geophysical Research Letters*, *33*(13). Retrieved from https://agupubs.onlinelibrary.wiley.com/doi/abs/10.1029/2006GL026689 doi: https://doi.org/10.1029/2006GL026689

Reed, K. A., Goldenson, N., Grotjahn, R., Gutowski, W. J., Jagannathan, K., Jones, A. D., ... Zarzycki, C. M. (2022). Metrics as tools for bridging climate science and applications. *WIREs Climate Change*, *13*(6), e799. Retrieved from https://wires.onlinelibrary.wiley.com/doi/abs/10.1002/wcc.799 doi: https://doi.org/10.1002/wcc.799

Rhoades, A. M., Jones, A. D., Srivastava, A., Huang, H., O'Brien, T. A., Patricola, C. M., ... Zhou, Y. (2020). The shifting scales of western u.s. landfalling atmospheric rivers under climate change. *Geophysical Research Letters*, *47*(17), e2020GL089096. Retrieved from https://agupubs.onlinelibrary.wiley.com/doi/abs/10.1029/2020GL089096 (e2020GL089096 10.1029/2020GL089096) doi: https://doi.org/10.1029/2020GL089096

Rhoades, A. M., Zarzycki, C. M., Inda-Diaz, H. A., Ombadi, M., Pasquier, U., Srivastava, A., ... Jones, A. D. (2023). Recreating the california new year's flood event of 1997 in a regionally refined earth system model. *Journal of Advances in Modeling Earth Systems*, *15*(10), e2023MS003793. Retrieved from https://agupubs.onlinelibrary.wiley.com/doi/abs/10.1029/2023MS003793 (e2023MS003793 2023MS003793) doi: https://doi.org/10.1029/2023MS003793

Shojaeezadeh, S. A., Nikoo, M. R., McNamara, J. P., AghaKouchak, A., & Sadegh, M. (2018). Stochastic modeling of suspended sediment load in alluvial rivers. *Advances in Water Resources*, *119*, 188-196. Retrieved from https://www.sciencedirect.com/science/article/pii/S0309170818301866 doi: https://doi.org/10.1016/j.advwatres.2018.06.006

Shukla, S., Safeeq, M., AghaKouchak, A., Guan, K., & Funk, C. (2015). Temperature impacts on the water year 2014 drought in california. *Geophysical Research Letters*, *42*(11), 4384-4393. Retrieved from https://agupubs.onlinelibrary.wiley.com/doi/abs/10.1002/2015GL063666 doi: https://doi.org/10.1002/2015GL063666

Slivinski, L. C., Compo, G. P., Whitaker, J. S., Sardeshmukh, P. D., Giese, B. S., McColl, C., ... Wyszyński, P. (2019). Towards a more reliable historical reanalysis: Improvements for version 3 of the twentieth century reanalysis system. *Quarterly Journal of the Royal Meteorological Society*, *145*(724), 2876-2908. Retrieved from https://rmets.onlinelibrary.wiley.com/doi/abs/10.1002/qj.3598 doi: https://doi.org/10.1002/qj.3598

Smith, B. L., Yuter, S. E., Neiman, P. J., & Kingsmill, D. E. (2010). Water vapor

fluxes and orographic precipitation over northern california associated with a landfalling atmospheric river. *Monthly Weather Review*, *138*(1), 74 - 100. Retrieved from https://journals.ametsoc.org/view/journals/mwre/138/1/2009mwr2939.1.xml doi: https://doi.org/10.1175/2009MWR2939.1

Straus, D. M. (2018). Clustering techniques in climate analysis. In *Oxford research encyclopedia of climate science.* doi: https://doi.org/10.1093/acrefore/9780190228620.013.711

Swain, D. L., Langenbrunner, B., Neelin, J. D., & Hall, A. (2018). Increasing precipitation volatility in twenty-first-century california. *Nature Climate Change*, *8*(5), 427–433. doi: https://doi.org/10.1038/s41558-018-0140-y

Swain, D. L., Tsiang, M., Haugen, M., Singh, D., Charland, A., Rajaratnam, B., & Diffenbaugh, N. S. (2014). The extraordinary california drought of 2013/2014: Character, context, and the role of climate change. *Bulletin of the American Meteorological Society*, *95*(9), S3.

Wallace, J. M., & Gutzler, D. S. (1981). Teleconnections in the geopotential height field during the northern hemisphere winter. *Monthly Weather Review*, *109*(4), 784 - 812. Retrieved from https://journals.ametsoc.org/view/journals/mwre/109/4/1520-0493_1981_109_0784_titghf_2_0_co_2.xml doi: 10.1175/1520-0493(1981)109⟨0784:TITGHF⟩2.0.CO;2

Wernli, H., & Schwierz, C. (2006). Surface cyclones in the era-40 dataset (1958–2001). part i: Novel identification method and global climatology. *Journal of the Atmospheric Sciences*, *63*(10), 2486 - 2507. Retrieved from https://journals.ametsoc.org/view/journals/atsc/63/10/jas3766.1.xml doi: https://doi.org/10.1175/JAS3766.1

White, A. B., Moore, B. J., Gottas, D. J., & Neiman, P. J. (2019). Winter storm conditions leading to excessive runoff above california's oroville dam during january and february 2017. *Bulletin of the American Meteorological Society*, *100*(1), 55 - 70. Retrieved from https://journals.ametsoc.org/view/journals/bams/100/1/bams-d-18-0091.1.xml doi: https://doi.org/10.1175/BAMS-D-18-0091.1

Xie, P., Chen, M., Yang, S., Yatagai, A., Hayasaka, T., Fukushima, Y., & Liu, C. (2007). A gauge-based analysis of daily precipitation over east asia. *Journal of Hydrometeorology*, *8*(3), 607 - 626. Retrieved from https://journals.ametsoc.org/view/journals/hydr/8/3/jhm583_1.xml doi: https://doi.org/10.1175/JHM583.1

Zhao, Y., Xu, X., Li, J., Zhang, R., Kang, Y., Huang, W., ... Sun, X. (2019). The large-scale circulation patterns responsible for extreme precipitation over the north china plain in midsummer. *Journal of Geophysical Research: Atmospheres*, *124*(23), 12794-12809. Retrieved from https://agupubs.onlinelibrary.wiley.com/doi/abs/10.1029/2019JD030583 doi: https://doi.org/10.1029/2019JD030583

1158 # Supplemental Material

Table S1: Prediction skills in capturing observed extreme precipitation events ($> 95^{th}$ percentile) using LSMP indices (LSMPis) as predictors constructed for daily meteorological fields at lags 0 and 2 (in parenthesis). POD: probability of detection. FAR: false alarm ratio. TS: threat score. GSS: Gilbert skill score. PSS: Pierce skill score. AIC: Akaike Information Criteria. Training period: NDJFM of 1948-1982; verification period: NDJFM of 1982-2015. The variables shown are anomalies but the subscript 'a' has been removed for brevity here.

Data	hits	misses	FA	CN	POD	FAR	TS	GSS	PSS	AIC
					IVT					
Training	217 (190)	27 (54)	762 (1387)	4136 (3509)	0.89 (0.78)	0.78 (0.88)	0.22 (0.12)	0.18 (0.07)	0.73 (0.5)	37373 (40789)
Verification	213 (196)	32 (49)	996 (1530)	3750 (3214)	0.87 (0.8)	0.82 (0.89)	0.17 (0.11)	0.13 (0.07)	0.66 (0.48)	36111 (38485)
					PW					
Training	217 (190)	27 (54)	998 (1419)	3900 (3477)	0.89 (0.78)	0.82 (0.88)	0.17 (0.11)	0.13 (0.07)	0.69 (0.49)	38523 (41323)
Verification	209 (167)	36 (78)	1227 (1524)	3519 (3220)	0.85 (0.68)	0.85 (0.9)	0.14 (0.09)	0.1 (0.05)	0.59 (0.36)	37280 (39505)
					U850					
Training	215 (188)	29 (56)	1128 (1510)	3770 (3386)	0.88 (0.77)	0.84 (0.89)	0.16 (0.11)	0.12 (0.06)	0.65 (0.46)	39329 (41166)
Verification	205 (189)	40 (56)	1241 (1462)	3505 (3282)	0.84 (0.77)	0.86 (0.89)	0.14 (0.11)	0.09 (0.07)	0.58 (0.46)	37505 (38621)
					SLP					
Training	209 (173)	35 (71)	1122 (1595)	3776 (3301)	0.86 (0.71)	0.84 (0.9)	0.15 (0.09)	0.11 (0.05)	0.63 (0.38)	39654 (42108)
Verificatio	204 (175)	41 (70)	1227 (1443)	3519 (3301)	0.83 (0.71)	0.86 (0.89)	0.14 (0.1)	0.1 (0.06)	0.57 (0.41)	37350 (39438)
					Z500					
Training	212 (175)	32 (69)	1261 (1649)	3637 (3247)	0.87 (0.72)	0.86 (0.9)	0.14 (0.09)	0.1 (0.05)	0.61 (0.38)	39895 (42154)
Verification	205 (181)	40 (64)	1276 (1556)	3470 (3188)	0.84 (0.74)	0.86 (0.9)	0.13 (0.1)	0.09 (0.06)	0.57 (0.41)	37623 (39415)
					V850					
Training	205 (186)	39 (58)	1121 (1529)	3777 (3367)	0.84 (0.76)	0.85 (0.89)	0.15 (0.1)	0.11 (0.06)	0.61 (0.45)	39949 (41751)
Verification	200 (170)	45 (75)	1368 (1569)	3378 (3175)	0.82 (0.69)	0.87 (0.9)	0.12 (0.09)	0.08 (0.05)	0.53 (0.36)	38219 (39377)
					T500					
Training	188 (154)	56 (90)	1431 (1732)	3467 (3164)	0.77 (0.63)	0.88 (0.92)	0.11 (0.08)	0.07 (0.03)	0.48 (0.28)	41175 (42732)
Verification	181 (155)	64 (90)	1793 (1939)	2953 (2805)	0.74 (0.63)	0.91 (0.93)	0.09 (0.07)	0.04 (0.03)	0.36 (0.22)	39368 (40430)
					Ts					
Training	186 (144)	58 (100)	1679 (1891)	3219 (3005)	0.76 (0.59)	0.9 (0.93)	0.1 (0.07)	0.05 (0.02)	0.42 (0.2)	41376 (43054)
Verification	194 (127)	51 (118)	1829 (1817)	2917 (2927)	0.79 (0.52)	0.9 (0.93)	0.09 (0.06)	0.05 (0.02)	0.41 (0.14)	39196 (40733)
					T850					
Training	186 (149)	58 (95)	1555 (1758)	3343 (3138)	0.76 (0.61)	0.89 (0.92)	0.1 (0.07)	0.06 (0.03)	0.44 (0.25)	41419 (42871)
Verification	196 (142)	49 (103)	1794 (2025)	2952 (2719)	0.8 (0.58)	0.9 (0.93)	0.1 (0.06)	0.05 (0.02)	0.42 (0.15)	39192 (40633)

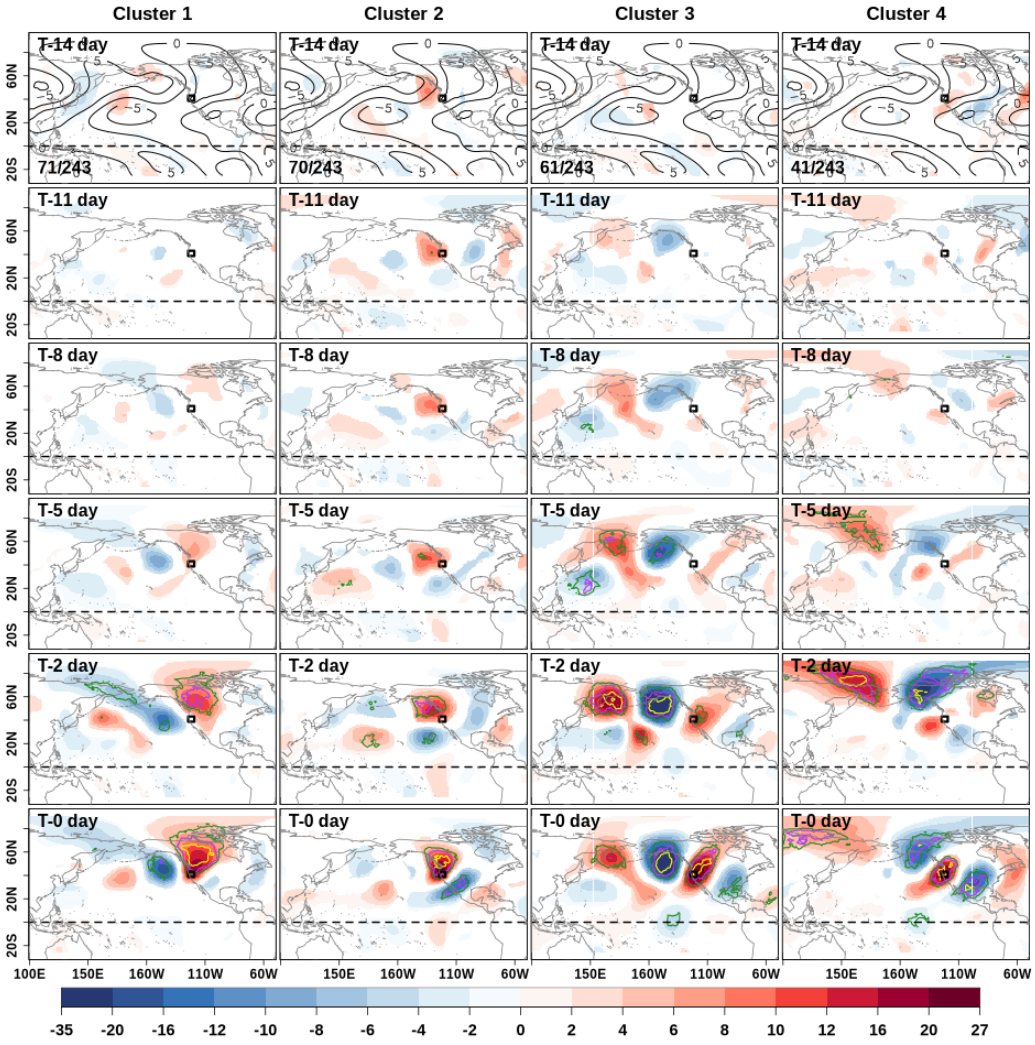

Figure S1: Evolution of 200hPa meridional wind anomalies (unit: m/s). Shaded areas show anomalies significant at the 5% level. Contours show the consistency of the anomaly pattern. Green, magenta, and yellow contours show that at least 80%, 87.5%, and 95% of the cluster members have the same sign of anomalies, respectively. Solid black contours (contour interval: 5 m/s) in the top rows show the climatological meridional wind. The ratio in the lower-left corner in the top rows shows the number of events in that cluster divided by the total number of events. The black rectangle indicates the NorCal region.

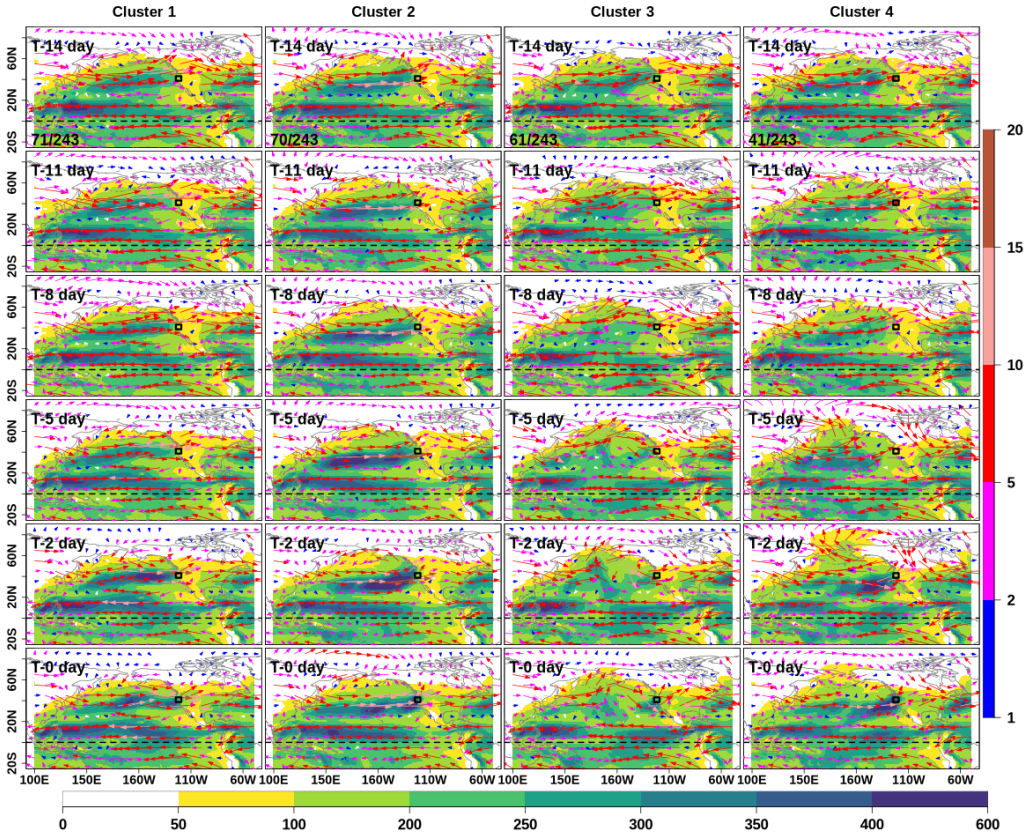

Figure S2: Same as Fig. S1 but for the evolution of total integrated vapor transport (shading; unit: kg/m-s). The vectors show the 850 hPa wind (unit: m/s). The bottom color bar pertains to the IVT, and the vertical color bar to the 850 hPa wind.

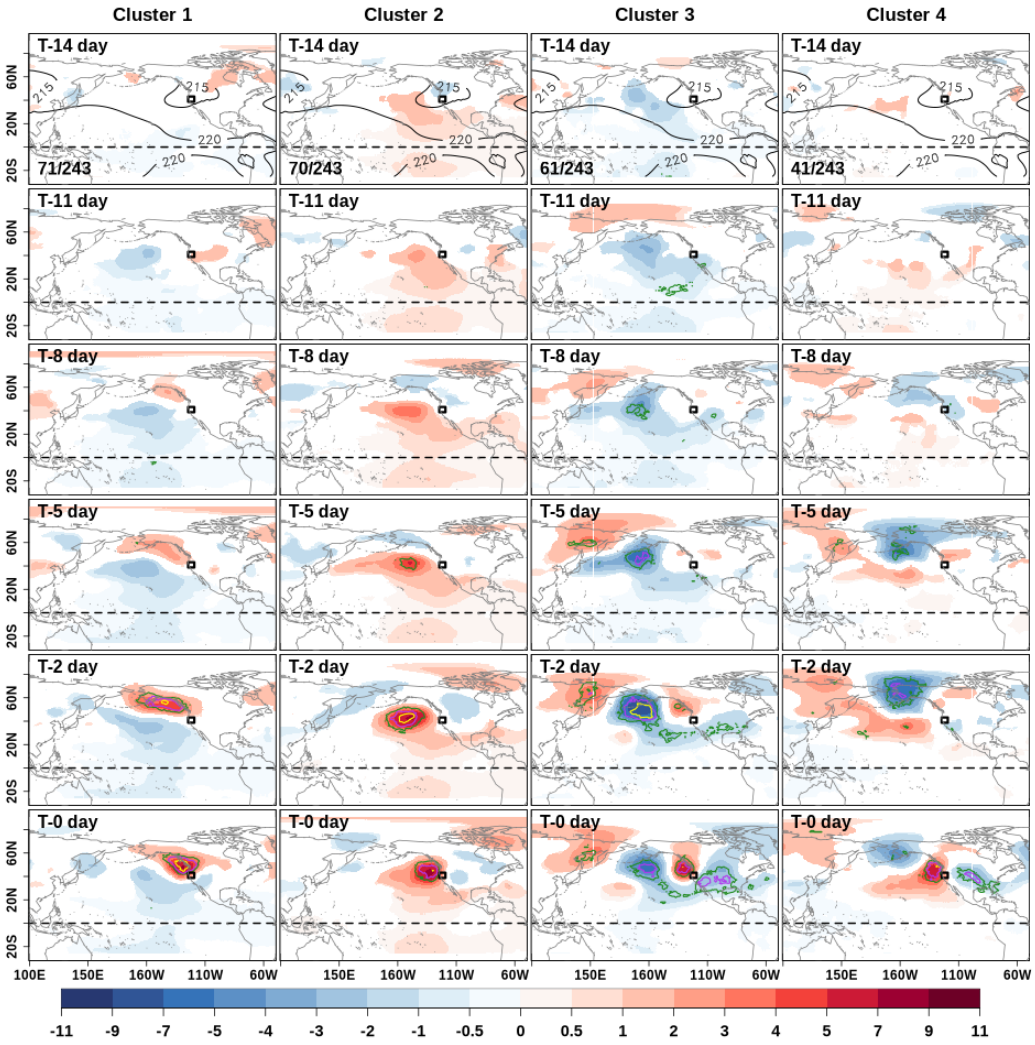

Figure S3: Same as Fig. S1 but for the evolution of the 200 hPa air temperature anomaly (unit: K). Solid black contours (contour interval: 5 K) in the top rows show the climatological 200 hPa air temperature anomaly.

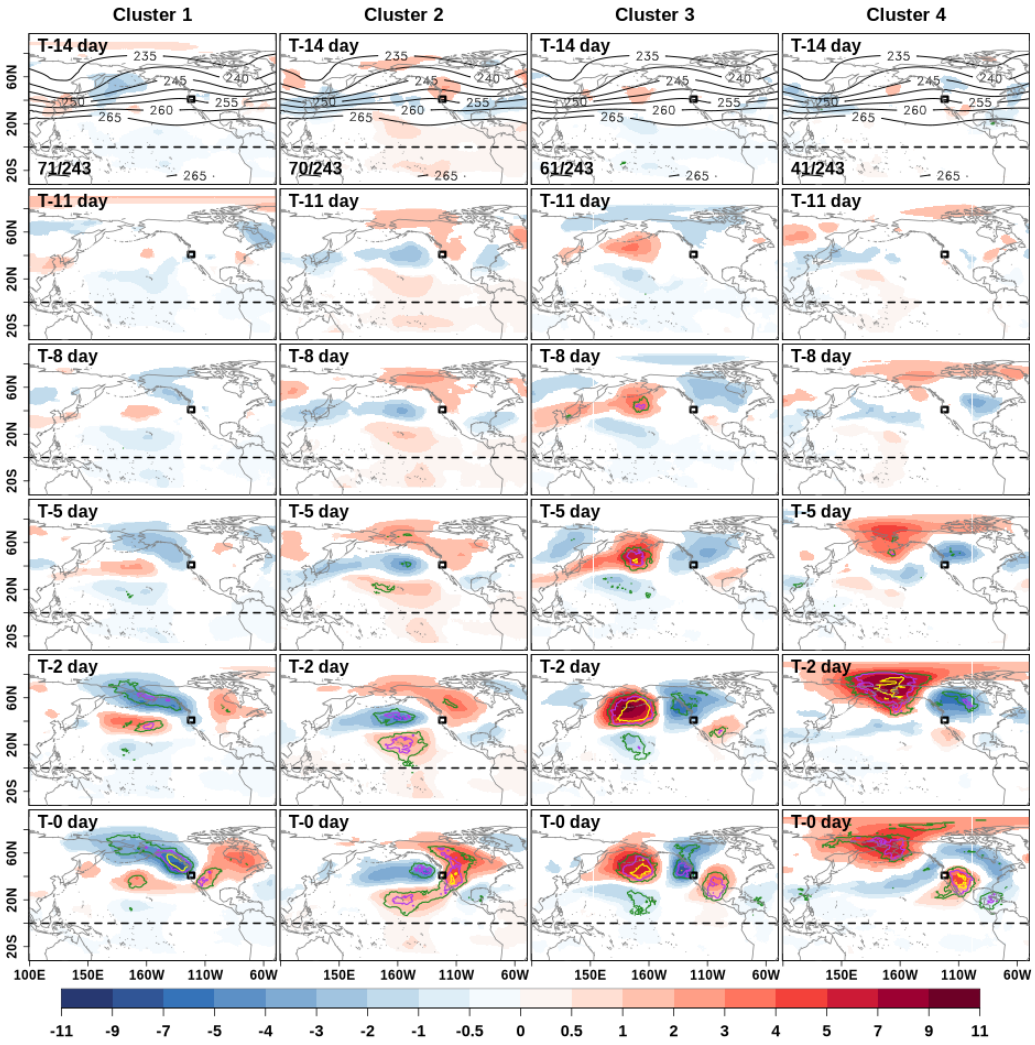

Figure S4: Same as Fig. S1 but for the evolution of the 500hPa air temperature anomaly (unit: K). Solid black contours (contour interval: 5K) in the top rows show the climatological 500 hPa air temperature anomaly.

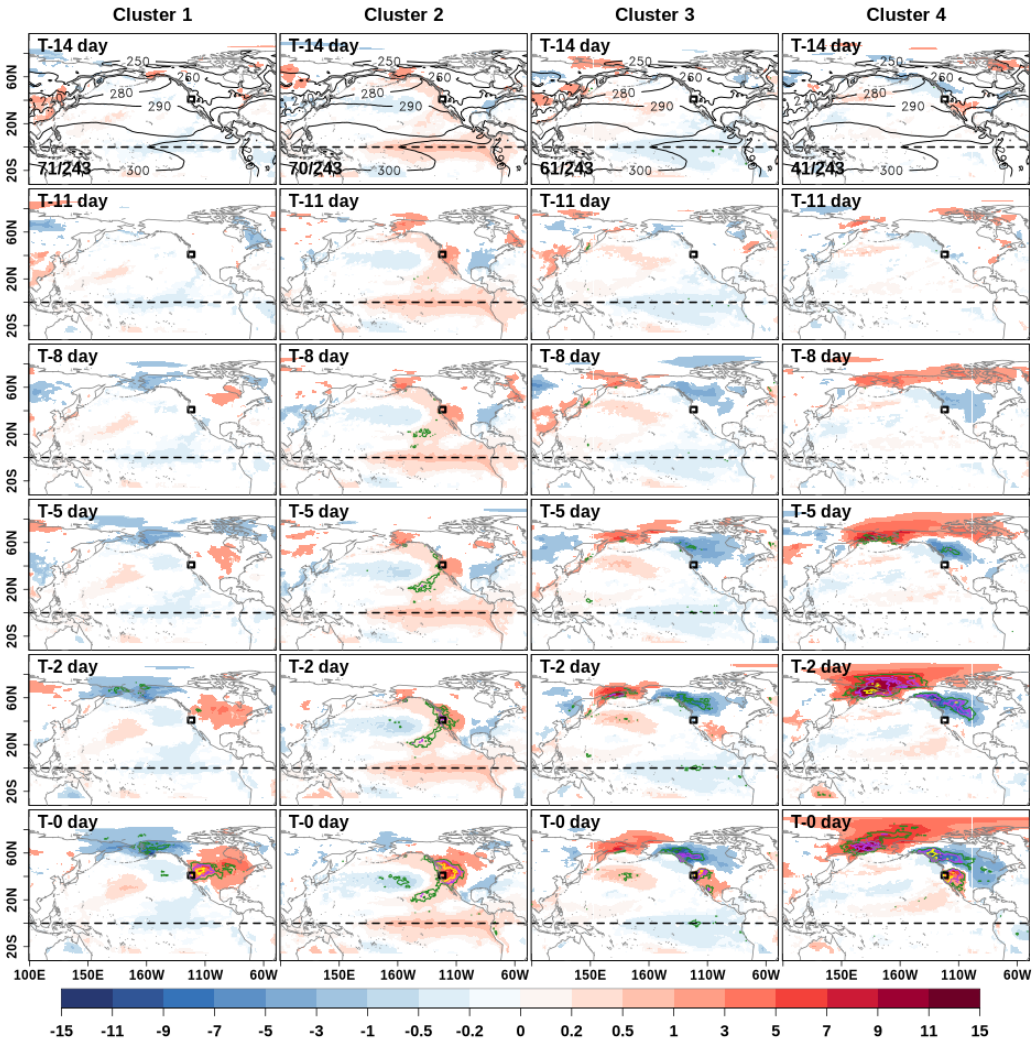

Figure S5: Same as Fig. S1 but for the evolution of the skin temperature anomalies (unit: K). Solid black contours (contour interval: 10 K) in the top rows show the climatological skin temperature anomalies.

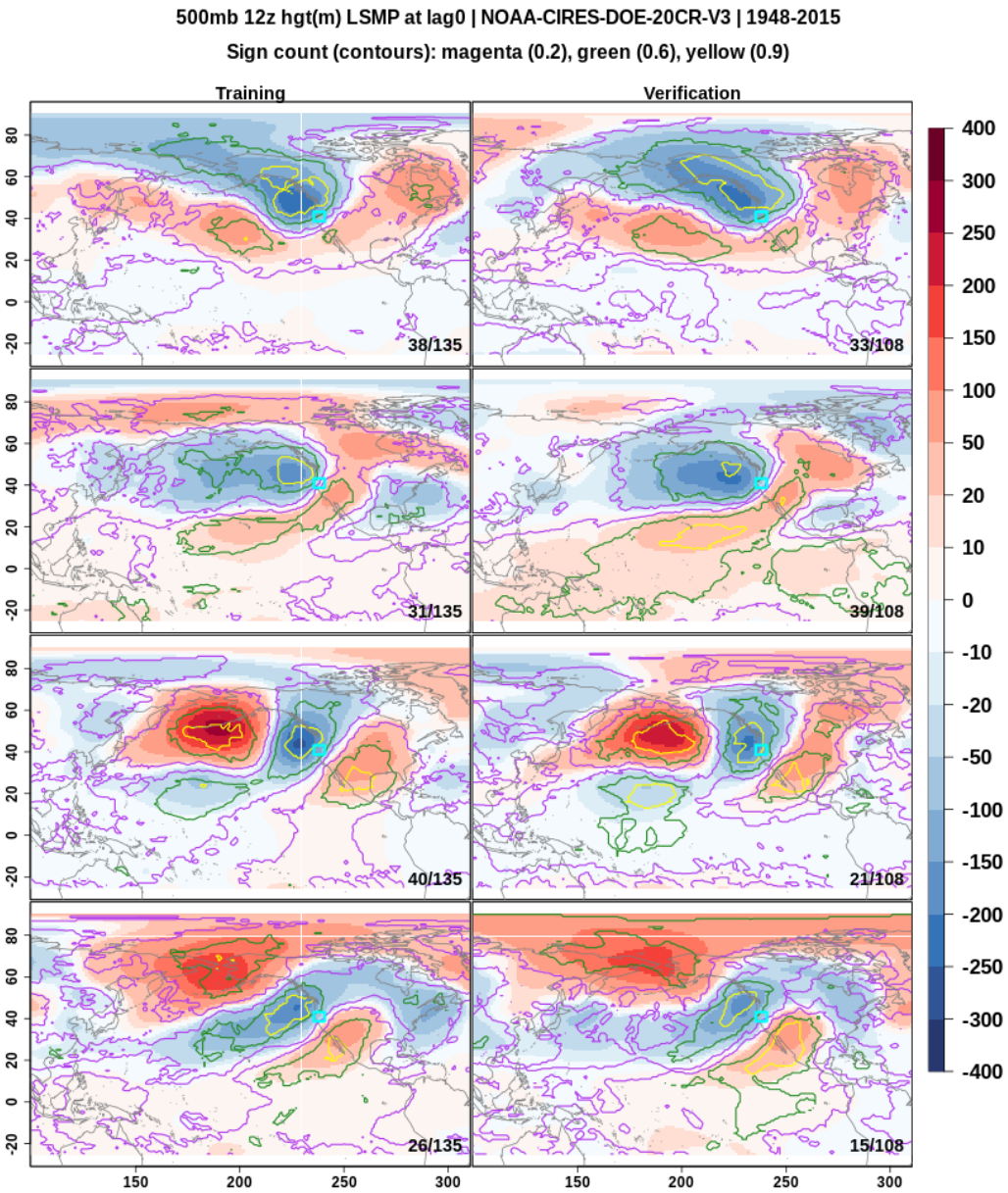

Figure S6: LSMP clusters for lag 0 500mb geopotential height anomalies during months November-March. The left panel shows the LSMP for the training period (1948-1982) and the right panel shows the LSMP for the verification period (1982-2015). Unit:m.